Decoding Spine Nanostructure in Mental Disorders Reveals a Schizophrenia-Linked Role for Ecrg4

Yutaro Kashiwagi[1], Qingrui Liu[1], Yasuhiro Go[2, 3,4], Ryo Saito[5], Atsu Aiba[5], Takanobu Nakazawa[6], and Shigeo Okabe[1,7,*]

[1]Department of Cellular Neurobiology, Graduate School of Medicine, the University of Tokyo, Tokyo 113-0033, Japan

[2]Graduate School of Information Science, University of Hyogo, Kobe 650-0047, Japan

[3]National Institute for Physiological Sciences (NIPS), National Institutes of Natural Sciences, Okazaki 444-8585, Japan

[4]Exploratory Research Center on Life and Living Systems (ExCELLS), National Institutes of Natural Sciences, Okazaki 444-8585, Japan

[5]Laboratory of Animal Resources, Center for Disease Biology and Integrated Medicine, Graduate School of Medicine, the University of Tokyo, Tokyo, 113-0033, Japan

[6]Department of Bioscience, Faculty of Life Sciences, Tokyo University of Agriculture, Tokyo 156-8502, Japan

[7]RIKEN Center for Brain Science, Saitama 351-0198, Japan

[*]Corresponding author: Shigeo Okabe

Department of Cellular Neurobiology, Graduate School of Medicine, the University of Tokyo, 7-3-1 Hongo Bunkyo-ku 113-0033 Tokyo, Japan

Phone: 81-3-5841-1928 Fax: 81-3-5841-1930

E-mail: okabe@m.u-tokyo.ac.jp

Abstract

Dendritic spine dysfunction may contribute to the etiology and symptom expression of neuropsychiatric disorders. The intimate relationship between spine morphology and function suggests that decoding disease-related abnormalities from spine morphology can aid in developing synapse-targeted interventions. Here, we describe a population analysis of dendritic spine nanostructure applied to the objective grouping of multiple mouse models of neuropsychiatric disorders. This method has identified two major groups of spine phenotypes linked to schizophrenia and autism spectrum disorder (ASD). An increase in spine subpopulation with small volumes characterized the spines of schizophrenia mouse models, whereas a spine subset with large volumes increased in ASD models. Schizophrenia mouse models showed higher similarity in spine morphology, which was caused by a reduced speed of nascent spine growth. The expression of Ecrg4, a gene encoding small secretory peptides, was increased in schizophrenia mouse models, and functional studies confirmed its critical involvement in impaired spine dynamics and shape in schizophrenia mouse models. These results suggest that the population-level spine analysis provides rich information about the heterogeneous spine pathology, which facilitates identification of new molecular targets related to core synaptic dysfunction.

Introduction

Information processing in the neocortex and hippocampus relies on fast excitatory synaptic transmission between pyramidal neurons. Many excitatory synapses that release glutamate project onto tiny structures protruding from dendritic shafts termed spines, and the morphological properties of these spines strongly influence synaptic transmission and function, including the activity-dependent synaptic plasticity implicated in learning and memory[1,2]. In general, larger spines contain a greater number of glutamate receptors and are functionally stronger[3]. The morphological parameters defining spine shape, such as length, radius, and volume, are also highly dynamic. For instance, small nascent spines can be enlarged by high-frequency stimuli inducing long-term potentiation (LTP) of synaptic transmission[4,5]; alternatively, spine volume can be reduced by low-frequency stimuli that induce long-term depression (LTD)[5,6]. Due to these dynamic changes, spines on pyramidal neurons exhibit substantial morphological variation, even within the same dendritic branch. In addition to direct synaptic activation inducing LTP or LTD, spine morphology can be altered by cyclical hormonal changes, neuromodulators, and various activity-independent processes[7–10]. In turn, these changes in spine morphology are associated with marked changes in neural function and behavior.

Recent advances in super-resolution microscopy have provided new opportunities for the study of spine structural diversity and dynamics. A recent investigation using stimulated emission depletion (STED) imaging reported an increase in spine neck size after LTP, resulting in stronger electrical coupling between the spine head and dendritic shaft[11]. A structured illumination microscopy (SIM) imaging study of

70 cultured hippocampal neurons revealed expansion of the spine head convexity after
71 LTP induction[12], and suggested that this structural transformation may increase the
72 adhesion of presynaptic and postsynaptic membranes. SIM imaging has also been
73 applied to record the dynamic properties of spinules[13], thin protrusions extending from
74 existing spines that may function in secondary synapse formation. Collectively, these
75 reports implicate spine nanostructural dynamics in multiple core synaptic properties
76 and functions, including neurotransmission, mechanical stability, synaptogenesis, and
77 plasticity.

78 Genetic mutations and variants that disrupt synaptic function are strongly
79 implicated in the pathogenesis of neuropsychiatric disorders such as autism spectrum
80 disorder (ASD) and schizophrenia[14–20]. Based on these genomic aberrations, numerous
81 mouse models of ASD and schizophrenia have been established and subsequently
82 shown to harbor abnormalities in both spine morphology and physiology[19,21–24].
83 Moreover, several studies have reported synaptic dysfunction in neurons differentiated
84 from patient-derived pluripotent stem cells [25–28]. Schizophrenia and ASD share several
85 clinical features, suggesting common genetic risk factors and etiology[29,30]. However, a
86 diametrical model emphasizes the distinct social-cognitive properties of these two
87 major psychiatric disorders[31,32]. Both ASD and schizophrenia also show highly
88 heterogeneous clinical phenotypes, potentially stemming from distinct pathogenic
89 processes within disease categories. Therefore, in addition to clinical features,
90 comparative biological phenotyping of multiple ASD and schizophrenia models may
91 reveal shared as well as disease-specific pathogenic processes.

92 Genetic studies on ASD and schizophrenia have identified copy-number

93 variants and protein-disrupting single-nucleotide variants that confer higher disease
94 risk, and mouse models harboring these genetic abnormalities frequently exhibit
95 behavioral and neurological features resembling those of the clinical conditions (termed
96 endophenotypes)[19,33]. However, there are only a limited number of studies objectively
97 comparing phenotypes related to synaptic structure and function between disease
98 models. An *in vivo* two-photon imaging study reported accelerated spine turnover in
99 three genetically distinct ASD mouse models [34]. Also, multiple ASD mouse models
100 were found to exhibit a similar imbalance in the activity of excitatory and inhibitory
101 neurons[35]. These studies support the idea that distinct genetic mutations may induce
102 similar synaptic and circuit phenotypes in ASD mouse models. However, differences in
103 synaptic properties between ASD and schizophrenia have not yet been
104 comprehensively examined.

105 In this study, we developed an objective method for identifying population-
106 level differences in spine nanostructure. This method, which has been applied to
107 multiple mouse models of psychiatric disorders, identified two distinct groups
108 corresponding to ASD and schizophrenia. An increase in a specific spine
109 subpopulation with small volumes characterized the spines of schizophrenia mouse
110 models. In turn, ASD mouse models showed a tendency of decreasing spine
111 subpopulation with small volumes. The schizophrenia-related phenotype was
112 associated with slower volume growth and enhanced turnover. Further gene
113 expression analysis identified the overexpression of Ecrg4, a gene encoding a
114 precursor of hormone-like peptides, as a candidate mediator of this schizophrenia-
115 associated spine phenotype. Population-level analysis of spine nanostructures is a
116 powerful approach for understanding heterogeneous synaptic impairments in

117 psychiatric disorders.

118

Results

Spine nanostructure imaging and generation of the spine density plot

We have designed a method for objectively comparing spine properties among multiple mouse models of psychiatric disorders at the population level using SIM imaging. Previous results demonstrated that high-resolution SIM images of dendritic spines in cultured hippocampal neurons can provide reliable information about spine size and morphological properties[12]. In the current study, the analytical procedures for SIM images were further improved for quantitative comparisons. Three-dimensional SIM images of dendritic spines were captured in DiI-stained cultured neurons derived from control and disease-model mouse hippocampus (Figure 1A). This staining procedure provided a better image quality than fluorescent protein-based labeling because of the higher fluorescence signal from the plasma membrane. SIM images were processed using custom-made scripts to identify and segment the individual dendritic spines (Figure 1B–D). We previously reported a set of scripts designed to isolate dendritic spines automatically[12]. However, the segmentation accuracy still necessitated manual inspection. In the newly developed scripts, we introduced a step for readjusting the spine–shaft boundary that enabled fully automated measurement of multiple morphological parameters, including length, surface area, and volume. In addition, the isolated spines were further divided into 160-nm thick longitudinal segments for calculating a total of 64 shape descriptors.

Spine shape parameters measured by conventional methods are difficult to compare directly when images are obtained from multiple independent experiments.

142 This problem is caused by several reasons, but the main factors are variability in image
143 intensity, signal-to-noise ratio, and image aberration introduced by unoptimized
144 imaging conditions. To test the stability of the SIM-based spine imaging, we compared
145 the spine size distribution in four samples prepared at time points separated by >2
146 months from each other (Supplementary Figure 1). The cumulative distribution curves
147 of the four datasets showed extensive overlap, confirming the reproducibility of the
148 SIM-based spine shape measurements using independent culture samples.

149 Another technical issue related to the comparison of spine shape is the
150 heterogeneity of spine shape and the absence of defined subclasses. Population-level
151 spine analysis, therefore, requires a new strategy that enables objective comparisons
152 of large numbers of spines with a continuum of morphologic features. We previously
153 demonstrated that principal component analysis (PCA) was effective for comparing
154 high-dimensional spine shape features (descriptors) in a feature space with reduced
155 dimensions[12]. Indeed, a PCA-based dimensional reduction applied to a large number of
156 spines based on their descriptors generated a two-dimensional plot of spine shape that
157 closely matched conventional spine subtypes, such as thin, mushroom, and stubby
158 (Figure 1E). To objectively compare the two spine datasets (control and disease
159 model), we first generated plots of relative spine densities (number per area in feature
160 space) mapped to 80 × 80 square blocks (Figure 1F), and then subtracted the
161 corresponding plot pairs defined by genotype (control vs. mutant) or culture conditions.
162 The resulting subtracted density plots contain comprehensive information about the
163 differences in relative spine numbers with similar shape properties.

164

165 **Comparison and grouping of multiple mouse models based on morphological**
166 **spine similarity**

167 The subtracted density plots contain rich information about the population-level
168 differences in spine shape between samples. Therefore, the generation and
169 comparison of the plots for both ASD and schizophrenia mouse models will be useful
170 for their unbiased grouping. We selected the following eight representative mouse
171 models harboring either copy-number variation or single gene mutations associated
172 with psychiatric disorders: male hemizygous or female homozygous mutant mice for
173 neuroligin-3 R451C mutation (Nlgn3$^{R451C/(y\ or\ R451C)}$)[36,37], heterozygous Syngap1 mutant
174 mice (Syngap1$^{+/-}$)[38], heterozygous POGZ mutant mice (POGZ$^{Q1038R/+}$)[39], mice paternal
175 duplication of chromosome 7C (15q11-13$^{dup/+}$) corresponding to human 15q11-13
176 duplication[40], mice with heterozygous deletion of chromosome 16B2,3 (3q29$^{del/+}$)
177 corresponding to human 3q29 deletion[41], mice heterozygous for deletion on
178 chromosome 16qA13 (22q11.2$^{del/+}$) corresponding to 1.5 Mb deletion on human
179 22q11.2[42], mice heterozygous for Setd1a mutation (Setd1a$^{+/-}$)[43], and Ca^{2+}/calmodulin-
180 dependent protein kinase IIα kinase-dead mutant mice (CaMKIIα$^{K42R/K42R}$)[44]. Previous
181 studies on these mouse models confirmed the presence of multiple sensory, memory,
182 and social endophenotypes of psychiatric disorders compared to controls. Of these,
183 Nlgn3$^{R451C/(y\ or\ R451C)}$, POGZ$^{Q1038R/+}$, and 15q11-13$^{dup/+}$ models mimic genetic variations
184 found in ASD. Human mutations in the SYNGAP1 gene are associated with mental
185 retardation (MR) and autistic behaviors. The 3q29$^{del/+}$, 22q11.2$^{del/+}$, and Setd1a$^{+/-}$
186 models harbor genetic mutations associated with higher schizophrenia risk. The
187 CaMKIIα$^{K42R/K42R}$ mutation does not correspond to any known human genetic variant,
188 but CaMKII-related signaling pathway disruption has been implicated in the working

189 memory deficits found in schizophrenia patients[45,46]. Therefore, these mouse models
190 cover a broad spectrum of human genetic aberrations associated with psychiatric
191 disorders. Direct comparison of spine phenotypes could therefore provide important
192 clues to underlying shared and disease-specific synaptic pathologies.

193 For these comparisons, we prepared three independent culture samples from
194 each control–mutant pair and obtained 700–1,500 3D-SIM spine images 3 weeks after
195 plating for both mutant and control samples (Nlgn3$^{R451C/(y\ or\ R451C)}$, n = 1,134 and 1,204;
196 Syngap1$^{+/-}$, n = 991 and 1,371; POGZ$^{Q1038R/+}$, n = 1,341 and 1,271; 15q11-13$^{dup/+}$, n =
197 1,208 and 1,099; 3q29$^{del/+}$, n = 1,429 and 1,408; 22q11.2$^{del/+}$, n = 1,143 and 914;
198 Setd1a$^{+/-}$, n = 1,381 and 1,405; CaMKIIα$^{K42R/K42R}$; n = 880 and 763, control and mutant,
199 respectively). Initial comparison of the cumulative frequency plots for spine length,
200 spine surface area, and spine volume alone did not provide sufficient information to
201 infer their structural similarity (Supplementary Figure 2), indicating that simple structural
202 parameters are not effective in identifying disease-specific spine shape characteristics.
203 We next generated subtracted density plots from 8 mouse models. These plots were
204 variable, but there were certain similarities between the specific mutants (Figure 2A).
205 We evaluated pairwise similarities by calculating the 2D cross-correlations of the
206 subtracted density plots. The matrix of these 2D cross-correlation values yielded two
207 major groups with high within-group similarity (Figure 2B), and the presence of these
208 two groups was further confirmed by unbiased clustering analysis (Figure 2C). The first
209 group contained the ASD models Nlgn3$^{R451C/(y\ or\ R451C)}$, Syngap1$^{+/-}$, and POGZ$^{Q1038R/+}$,
210 while the second group consisted of the schizophrenia models 3q29$^{del/+}$, 22q11.2$^{del/+}$,
211 Setd1a$^{+/-}$, and CaMKIIα$^{K42R/K42R}$. This result is striking, as it indicates that the
212 information of spine shape alone can tell whether the culture preparation is derived

213 from ASD or schizophrenia mouse models. It is also of note that there were greater
214 similarities among the schizophrenia mouse models than among the ASD mouse
215 models. This finding suggests a convergence of spine pathophysiology in the
216 schizophrenia mouse models.

217 In addition to the eight mouse models of psychiatric disorders, we generated
218 subtracted density plots for three additional conditions: immature culture samples (13
219 days in vitro, DIV), treatment with the AMPA subtype glutamate receptor blocker
220 CNQX, and treatment with the $GABA_A$ receptor blocker bicuculline (Figure 2A). The
221 subtracted density plots of the 13 DIV culture and CNQX treatment were similar to
222 those of the schizophrenia mouse models. This finding suggests that the hippocampal
223 synapses in mouse models of schizophrenia are immature and inactive. In contrast, the
224 subtracted density plot of the bicuculline-treated sample was distinct from that of both
225 the schizophrenia and ASD mouse models.

226

227 **Distinct spine shape between ASD and schizophrenia mouse models**

228 The subtracted density plots provide information about the structural properties of
229 specific spine subsets, which either increased or decreased in disease mouse models.
230 We first defined the areas within the plots where the control or mutant spines showed
231 higher density. Next, we extracted the spines in the control-enriched area (A) and the
232 mutant-enriched area (B), and compared the volumes and shape profiles of spines in
233 these areas. For the 22q11.2$^{del/+}$ schizophrenia mouse model, the control-enriched area
234 (A) contained larger spines than the mutant-enriched area (B) (Figure 3B, D, F, H, and
235 J). In contrast, the mutant-enriched area (B) of the Nlgn3$^{R451C/(y\ or\ R451C)}$ ASD mouse

236 model overlapped with the domain of large spines, while the control-enriched area (A)
237 contained smaller spines (Figure 3A, C, E, G, and I). These differences in population-
238 level spine properties between ASD and schizophrenia mouse models were relatively
239 consistent (Supplementary Figures 3–7) in that smaller spines were observed in
240 mutant-enriched areas of all four schizophrenia mouse models (3q29$^{del/+}$, 22q11.2$^{del/+}$,
241 Setd1a$^{+/-}$, and CaMKIIα$^{K42R/K42R}$) (Supplementary Figures 6), while large spines were
242 dominant in the mutant-enriched areas of the three ASD mouse models (Nlgn3$^{R451C/(y\ or}$
243 $^{R451C)}$, Syngap1$^{+/-,}$ and POGZ$^{Q1038R/+}$). The only exception was 15q11-13$^{dup/+}$, which
244 showed enrichment of small spines in the mutant-dominant area. The fractions of
245 spines present in the control-enriched area (A) and mutant-enriched area (B) were
246 substantial in all eight mouse models (fraction of spines in area A: 0.24 ± 0.058 for
247 controls, 0.20 ± 0.063 for mutants; fraction of spines in area B: 0.26 ± 0.057 for
248 controls, 0.31 ± 0.062 for mutants, mean±SD), indicating that despite broad value
249 spectra for all datasets, approximately half of the total spine population was within
250 either area (A) or (B) in data from both the control mice (0.50 ± 0.036, mean±SD) and
251 mutant mice (0.51 ± 0.031, mean±SD).

252

253 **Slow initial growth of dendritic spines in schizophrenia model mice**

254 The subtracted density plots indicate the common changes in the spine population of
255 the schizophrenia mouse models. The mutant-enriched areas correspond to the
256 specific spine population with small morphology, suggesting underlying dysfunction in
257 either generation of nascent spines or shrinkage of existing spines. To examine
258 potential abnormalities in spine dynamics, we performed time-lapse imaging of

259 hippocampal neuron cultures derived from two schizophrenia mouse models,
260 22q11.2$^{del/+}$ and Setd1a$^{+/-}$, and the Nlgn3$^{R451C/(y\ or\ R451C)}$ ASD mouse model as a
261 reference (Figure 4). Time-lapse imaging over 24 h captured numerous *de novo* spine
262 formation and spine loss events. Compared to control neurons, neurons from the two
263 schizophrenia models exhibited slower growth of nascent spines (Figure 5G–L). Spine
264 turnover rate was upregulated in these schizophrenia mouse models (Figure 5A and
265 B), while the ASD model did not show significant upregulation (Figure 5C). The slow
266 growth of spines in neurons from the schizophrenia mouse models was associated with
267 a longer lifetime of transient spines (Figure 5D and E) compared to the ASD model
268 (Figure 5F). Taken together, these results suggest that the slower growth of nascent
269 spines and instability of existing spines contribute to the development of schizophrenia-
270 related spine phenotypes.

271 To further examine the relationship between the spine growth rate and
272 lifetime, we performed simulations using the computational model shown in Figure 6A.
273 In this model, new spines appear randomly along the dendritic shaft according to a
274 density-dependent probability function, then increase in volume with speed V1 (phase
275 1), are eliminated with probability P1 (phase 2), and are converted to stable spines
276 upon reaching a volume threshold (phase 3). These stable spines are subsequently
277 destabilized with low probability P2 (phase 4) and start to shrink with speed V2 (phase
278 5). When these shrinking spines reach a threshold, they are permanently removed.
279 This model was run over 10 days of neuronal differentiation in culture (corresponding to
280 the period of spine density increase from 8 to 17 DIV) with 625 different combinations
281 of V1, V2, P1, and P2 to identify the combination with the best fit to the experimental
282 data for spine turnover of 15–18 DIV neurons derived from mutants 22q11.2$^{del/+}$,

283 Setd1a$^{+/-}$, and Nlgn3$^{R451C/(y\ or\ R451C)}$ over 24 h (Figure 6B). The best-fitted models all
284 yielded spine lifespan distributions matching observations of the three mouse mutants
285 (Figure 6C). The three characteristics of the spines in 22q11.2$^{del/+}$ and Setd1a$^{+/-}$ were
286 also preserved in the best-fitted model. First, the simulation showed higher turnover
287 rates for schizophrenia-related spines (21.4 ± 2.89% and 36.2 ± 4.16% for the best-
288 fitted models for the control and the schizophrenia mouse models, Supplementary
289 Figure 8A), as in the case of experimental data (Figure 5A and B). Second, spine
290 density in the schizophrenia mouse models was lower in both the simulation and
291 experimental data (simulation; 0.57 ± 0.029 /μm and 0.40 ± 0.027 /μm for the control
292 and the best-fitted for schizophrenia, shown in Supplementary Figure 8B, experiment;
293 0.69 ± 0.17 /μm and 0.56 ± 0.20 /μm for the control and 22q11.2$^{del/+}$, 0.70 ± 0.15 /μm
294 and 0.64 ± 0.16 /μm for the control and Setd1a$^{+/-}$). Third, the size of transient spines
295 was smaller in the schizophrenia mouse models in the simulation (0.33 ± 0.033 and
296 0.20 ± 0.024 (a.u.) for the control and the best-fitted for schizophrenia, Supplementary
297 Figure 8C), consistent with the data of spine nanostructure (Figure 3H).

298 After the selection of the best-fitted parameters for three mouse models, we
299 compared the optimal values of V1, V2, P1, and P2 between mouse models (Figure
300 6D). The nascent spine volume increase (V1) was slower in the schizophrenia models
301 compared to corresponding controls. In turn, the probability of nascent spine loss (P1)
302 was higher in the ASD model. In all three disease models, the probability of spine
303 destabilization (P2) was moderately higher than that in the corresponding controls.
304 These results suggest that a slow spine volume increase in schizophrenia model mice
305 results in the accumulation of nascent spines with smaller volumes. On the other hand,
306 the spines of ASD model mice grow at a rate similar to that of control spines, but are

307 more likely to be eliminated both in the nascent stage and after maturation.

308 The simulated trajectory plots of individual spines along the dendritic shaft
309 using the best-fit parameters also reflected the differential patterns of spine turnover in
310 culture preparations derived from the control and schizophrenia model mice (Figure
311 6E). In culture preparations derived from schizophrenia mouse models, there were
312 fewer spines with a lifetime longer than 2 or 3 days, while there was a greater number
313 of spines formed and eliminated within 24 h. This increase in the number of less stable
314 spines explains the pattern of spine lifetime in Figure 5D and E. In summary, these
315 simulations suggest that reduced spine maturation rate can account for the three key
316 properties of schizophrenia-related spines：the greater number of small volume
317 spines, the enhanced turnover, and the reduction in spine density observed in
318 schizophrenia model mice.

319

320 **Screening of molecules responsible for altered spine properties in schizophrenia**
321 **mouse models**

322 Both SIM-based imaging and time-lapse imaging suggest that the initial growth phase
323 of spines is slower in schizophrenia model mice. To identify candidate genes that may
324 contribute to this growth impairment, we performed RNA sequencing of libraries
325 derived from the cultured neurons of eight psychiatric disorder mouse models and
326 corresponding controls, and filtered the results for differentially expressed genes
327 (DEGs). The DEGs specific to more than two schizophrenia-related mouse models are
328 listed in Supplementary Figure 9. In the hippocampi of schizophrenia model mice, the
329 expression levels of Met, Osr1, Arhgap15, and Rnf170-ps were downregulated, while

330 Cip4, Ecrg4, and Npas4 expression levels were upregulated. The majority of these
331 DEGs have been previously implicated in the pathology of schizophrenia (Met)[47],
332 synaptic plasticity (Npas4)[48,49], or signaling pathways in the nervous system
333 (Arhgap15[50], Cip4[51], and Ecrg4[52]).

334 If these genes do regulate spines in schizophrenia mouse models,
335 manipulation of these genes in wild-type neurons may induce a spine phenotype
336 similar to schizophrenia mouse models. To test this possibility, we downregulated Met
337 and Arhgap15, and upregulated Cip4, Ecrg4, and Npas4 in separate wild-type
338 hippocampal neuron cultures and measured spine dynamics using time-lapse imaging.
339 Ecrg4 was the only DEG that modulated spine dynamics in the predicted direction
340 (Figure 7A and B). Thus, the aberrant expression of Ecrg4 may be related to the spine
341 phenotype of schizophrenia model mice.

342 Ecrg4 encodes a precursor protein that yields several short hormone-like
343 peptides via multiple cleavage sites[53]. Ecrg4 has been reported to function in cell
344 proliferation, inflammation, and tumor suppression. However, there is limited
345 information on the neuronal functions of Ecrg4. Therefore, we further analyzed the
346 cellular distribution of Ecrg4 in wild-type hippocampal neurons to assess its potential
347 functions at synapses. The Ecrg4 protein was detected in the membrane fraction of
348 cultured hippocampal neurons (Supplementary Figure 10A). In addition, HA-tagged
349 Ecrg4 showed punctate localization patterns within the neuronal cytoplasm (Figure 7C).
350 A fraction of HA-tagged Ecrg4 puncta localized at axonal varicosities (arrowheads) or
351 dendritic spines (arrows), together with some extracellular clusters (asterisks). HA-
352 tagged Ecrg4 also colocalized with GFP-tagged neuropeptide Y (NPY) (Supplementary

353 Figure 10B and C), suggesting transport in dense-core vesicles. Surface labeling of live
354 cells also revealed clusters of Ecrg4 on axonal boutons and dendritic spines
355 (Supplementary Figure 10D and E), supporting active exocytosis and tethering via its
356 binding partners to the plasma membrane. Collectively, these observations suggest
357 that the intracellular machinery for transporting and releasing Ecrg4 may be actively
358 involved in the regulation of synapse formation and maturation.

359

360 **Rescue of the synaptic phenotype in schizophrenia mouse models by Ecrg4**
361 **suppression**

362 The spatial localization of Ecrg4 protein in wild-type neurons and upregulated gene
363 expression in the hippocampus of schizophrenia model mice strongly suggest a
364 contribution to the observed spine abnormalities. To examine this possibility, we tested
365 whether Ecrg4 suppression rescues the synaptic phenotype of neurons derived from
366 schizophrenia mouse models. We introduced a GFP expression plasmid along with the
367 Ecrg4-shRNA plasmid or the control shRNA plasmid into neurons derived from
368 22q11.2$^{del/+}$ and Setd1a$^{+/-}$ mice (Figure 8A and Supplementary Figure 10G). While the
369 spine density plots generated from GFP-expressing neurons differed from those
370 generated from DiI-labeled neurons, the subtracted (differential) distribution pattern
371 between Ecrg4 shRNA and control shRNA neurons showed an increase in the larger
372 volume spine fraction (Figure 8B), suggesting that Ecrg4 suppression reversed the
373 spine phenotype observed in naïve neurons from schizophrenia model mice. In
374 contrast, the subtracted density plot between control shRNA-expressing neurons from
375 schizophrenia model mice and wild-type mice revealed a reduction in the fraction of

376 large volume spines (Supplementary Figure 11), consistent with comparisons of DiI-
377 labeled naïve neurons from these genotypes. These data support the idea that the
378 shRNA-mediated downregulation of Ecrg4 can rescue the spine shape impairment
379 observed in schizophrenia mouse models.
380

381 **Discussion**

382 We developed an objective method for identifying population-level differences in spine
383 nanostructures and applied it to cultured hippocampal neurons derived from multiple
384 mouse models of psychiatric disorders. We succeeded in identifying two distinct groups
385 of mouse models according to the population-level spine properties. Notably, these two
386 objectively identified groups correspond to mouse models with ASD-related gene
387 mutations and schizophrenia-related gene mutations. The higher fraction of small spine
388 population was the common characteristics of schizophrenia mouse models. Time-
389 lapse imaging of spine dynamics revealed that this smaller spine phenotype is
390 associated with a reduced speed of volume increase and enhanced turnover.
391 Screening for genes differentially expressed between mutant and control mice
392 identified Ecrg4 overexpression as a potential molecular mechanism contributing to the
393 schizophrenia spine phenotype. Indeed, suppression of Ecrg4 expression normalized
394 the spine phenotype in neurons derived from schizophrenia mouse models. These
395 findings support population-level analysis of spine nanostructures as a powerful
396 approach to elucidating the heterogeneous synaptic impairments underlying psychiatric
397 disorders.

398 Spine nanostructures provide information about developmental history,
399 previous activity, and current functional properties, but these fine structural details were
400 not accessible by conventional light microscopy. However, the recent advances of
401 super-resolution microscopy allow for the study of nanoscale spine morphology,
402 including in living preparations, and have revealed new structural features related to
403 important synaptic functions[11–13]. Another challenge to spine nanoscale imaging is the

404 structural heterogeneity across large spine populations, which may obscure important
405 population-level differences. Nonetheless, to understand the physiology and pathology
406 of neural networks, it is essential to obtain comprehensive information about a large
407 number of spines belonging to a single neuron and within local neuronal networks. We
408 previously reported a dimensional reduction technique coupled with machine learning
409 for evaluating spine properties at the population level [12], and have further refined this
410 method for the current investigation to extract population-level nanostructural features
411 of spines in multiple mouse models of psychiatric disorders. This method enabled us to
412 compare spine phenotypes among different mouse models objectively and group
413 disease models according to similarities and differences in the spine population.
414 Notably, the two identified groups corresponded to ASD-related gene mutations and
415 schizophrenia-related gene mutations, supporting the idea that population-level
416 analyses of spine nanostructures provide meaningful information on synaptic
417 abnormalities and dysfunction.

418 Population-level spine properties were more homogeneous in the
419 schizophrenia models (those with gene mutations implicated in schizophrenia) than in
420 the other 4 models studied, due in part to a shared tendency for smaller spines. In
421 contrast to these findings, several previous studies reported reduced numbers of small
422 spines in the postmortem cortical tissues of schizophrenia patients[22,54]. However, this
423 discrepancy may be attributed to developmental period as we examined fetal neuronal
424 spines after three weeks of *in vitro* differentiation while the aforementioned studies
425 included postmortem samples from patients over 40 years of age. One possible
426 scenario that may help unify these observations is that spine density is reduced in the
427 early postnatal period, and that this reduction evokes homeostatic plasticity, which in

428 turn reduces the fraction of small spines in later life. Another potential explanation is
429 that schizophrenia differentially affects regional spine properties (e.g., hippocampus
430 versus cortex). Previous *in vivo* two-photon imaging studies reported higher spine
431 turnover in the hippocampus than the cortex[55,56]. Therefore, the spine phenotype
432 identified in this study may be specific to hippocampal pyramidal neurons. Finally, while
433 the spine phenotype identified in the human postmortem brain undoubtedly resulted
434 from complex interactions among genetic background, environmental influences, and
435 regulation by nonneuronal cells, the data obtained from pure neuronal cultures are
436 more likely to reflect the direct impact of schizophrenia-related gene mutations on
437 synaptic properties. Therefore, our analytical method is advantageous in that it can
438 reveal the direct effects of genotype on spine phenotype, in this case identifying Ecrg4
439 overexpression as a potential driver of spine abnormalities in schizophrenia.

440 In addition to Ecrg4, these analyses identified several other DEGs common to
441 mice harboring schizophrenia-related mutations. However, time-lapse imaging
442 identified Ecrg4 as the most effective spine regulator, and we also found that Ecrg4
443 suppression reversed the abnormal spine phenotype in neurons derived from
444 schizophrenia model mice. Ecrg4 encodes a precursor protein of hormone-like
445 peptides [57]. Exogenously expressed Ecrg4 exhibited a punctate pattern in both axonal
446 and dendritic compartments, with a fraction of clusters present on the cell surface. This
447 observation indicates that Ecrg4 may be secreted locally by axons or dendrites,
448 thereby influencing synapses and adjacent neurons. Several signaling pathways act
449 downstream of Ecrg4, including the stress-related NF-κB pathway and PI3K/Akt/mTOR
450 pathway[53]. Ecrg4-derived peptides may also act through Toll-like receptor 4 (TLR4) or
451 multiple scavenger receptors, such as LOX1[57]. While Ecrg4-related signaling pathways

452 have been studied primarily in the context of inflammation and infection, there are few
453 studies on Ecrg4-related signaling pathways in neurons. However, an Ecrg4-deficient
454 mouse model demonstrated enhancements in neural stem cell proliferation and spatial
455 learning, suggesting that overexpression may disrupt hippocampal function[52]. We
456 suggest that Ecrg4 may be a critical regulator of neural development and
457 synaptogenesis in the hippocampus. Further studies are warranted to identify Ecrg4
458 receptors and downstream signaling pathways and to investigate the potential
459 dysfunction of these pathways in schizophrenia mouse models.

460 The nanoscale features of dendritic spines in ASD mouse models were more
461 variable than those in schizophrenia mouse models. This difference may be related to
462 the broader clinical spectrum of ASD, which ranges from mild impairments in social
463 skills to severe intellectual disability. It is possible that the four ASD mouse models
464 examined in this study, Nlgn3$^{R451C/(y\ or\ R451C)}$, Syngap1$^{+/-}$, POGZ$^{Q1038R/+}$, and 15q11-
465 13$^{dup/+}$, represent subgroups with different levels of hippocampal dysfunction. Among
466 the four ASD mouse models, 15q11-13$^{dup/+}$ showed population-level spine properties
467 closer to those of the schizophrenia models, and several clinical studies have reported
468 that CNVs in the 15q11-13 chromosomal region also confer an increased risk of
469 schizophrenia[58,59]. Analysis of the relationships between rare genetic variants and
470 synapse phenotypes in mouse models may contribute to the eventual categorization of
471 diseases based on neural circuit function rather than heterogenous and overlapping
472 symptoms.

473 The most important advantage of our analytical method is reproducibility,
474 despite the substantial heterogeneity in genotype and phenotype among these mouse

models. Thus, we are confident that the spine population analysis described here will help researchers in different laboratories obtain reliable and comprehensive information on spine properties. Further, this method could facilitate comparisons among a large number of mouse models harboring genetic mutations related to mental disorders. Spine morphology as measured in a reduced culture system can also demonstrate direct effects of gene mutations on neuronal phenotypes in the absence of indirect influences from nonneuronal cells or specific environments. Ultimately, these studies may identify the shared and specific pathogenic mechanisms of psychiatric disorders and lead to improved diagnosis and treatments.

486 **Materials and Methods**

487 **Neuronal culture and genotyping of tissue samples from genetically modified**

488 **mice**

489 The following mouse models of psychiatric disorders were examined for spine

490 nanostructural characteristics: male hemizygous or female homozygous neuroligin-3

491 R451C mutant (Nlgn3$^{R451C/(y\ or\ R451C)}$), heterozygous Syngap1 mutant mice (Syngap1$^{+/-}$),

492 heterozygous POGZ mutant mice (POGZ$^{Q1038R/+}$), mice with duplication of chromosome

493 7C (15q11-13$^{dup/+}$; corresponding to human 15q11-13 duplication), mice heterozygous

494 for deletion on chromosome 16B2,3 (3q29$^{del/+}$; corresponding to human 3q29 deletion),

495 mice heterozygous for deletion on chromosome 16qA13 (22q11.2$^{del/+}$; corresponding to

496 1.5 Mb deletion on human 22q11.2), mice heterozygous for Setd1a mutantion

497 (Setd1a$^{+/-}$), and Ca^{2+}/calmodulin-dependent protein kinase IIα kinase-dead mutant mice

498 (CaMKIIα$^{K42R/K42R}$). All animal experiments were reviewed and approved by Institutional

499 Animal Care and Use Committee of the University of Tokyo (permission number

500 A2023M031-02).

501 For the production of embryos harboring heterozygous mutations, male heterozygous

502 mutants were bred with wild-type female C57BL/6J mice (Japan SLC). For the

503 production of Nlgn3$^{R451C/(y\ or\ R451C)}$ embryos, Nlgn3$^{R451C/y}$ males and Nlgn3$^{R451C/+}$ females

504 were crossed. Embryos of CaMKIIα$^{K42R/K42R}$ mice were obtained by crossing

505 heterozygous CaMKIIα$^{K42R/+}$ males and females. Both male and female embryos were

506 used for the primary culture. Control cultures were prepared from embryos without

507 disease-related mutations on the background of C57BL/6J.

508 Genomic DNA was purified from E16 embryos prior to brain dissection using the

509 QuickGene DNA tissue kit (WAKO), and genotypes were determined by PCR using

510 either KapaTaq (Kapa Biosystems) or KOD FX Neo (TOYOBO) following the standard

511 protocols provided by the manufacturers. The primer sequences used for genotyping

512 were as follows:

513 Nlgn3$^{R451C/(y\ or\ R451C)}$ genotyping:

514 Sense primer: 5′- GGTCAGAGCTGTCATTGTCAC-3′

515 Antisense primer: 5’- TGTACCAGGAATGGGAAGCAG-3’

516 Syngap1$^{+/-}$ genotyping:

517 Sense primer for WT: 5’-GTCAGTGGGACATGGAAGTAG-3’

518 Sense primer for mutant: 5′-CTTCCTCGTGCTTTACGGTATC-3′

519 Antisense primer (common): 5’-CTGATCAGCCTGTCAGCAATG-3’

520 POGZ$^{Q1038R/+}$genotyping:

521 Sense primer for WT: 5’- TCTGTGAAGAAGCTTCGGGTAGTAC-3’

522 Antisense primer for WT: 5′-GTCTCCTCATTTACAGGGAGCT-3′

523 Sense primer for mutant: 5’- GCAGCGGCTCCCCGTTAAC-3’

524 Antisense primer for mutant: 5′- AGCGCACAGCCCACTCATAG-3′

525 15q11-13$^{dup/+}$ genotyping:

526 Sense primer: 5'- AGAGGAGGGCCTTACTAATTACTTA-3'

527 Antisense primer: 5′-ATATGTACTTTTGCATATAGTATAC -3′

528 3q29$^{del/+}$ genotyping:

529 Sense primer for WT: 5'- TTGGCACCACTCGCCCAAGTTATATCCACC-3'

530 Sense primer for mutant: 5’- CAAGGGGGAGGATTGGGAAGACAATAGCAG-3’

531 Antisense primer (common): 5’- GGTCATGCAAATTCTAGCAGTGAGTCATGAC-3’

532 22q11.2$^{del/+}$ genotyping:

533 Sense primer for WT: 5’- GAGAAAGTGGGTGGGAAGGC -3’

534 Antisense primer for WT: 5'- GTCCCTCGCCACAGTCATAA -3'

535 Sense primer for mutant: 5'- CTAAGGAATGGTTCCGGCCA -3'

536 Antisense primer for mutant: 5′- TTTCACGGAGGCGGTATTCA-3′

537 Setd1a$^{+/-}$ genotyping:

538 Sense primer: 5′-CTCGCCGCCATTTCTCTACATC-3′

539 Antisense primer: 5′-GTTCTGGAGGTTCTGGAGGTG-3′

540 CaMKIIα$^{K42R/K42R}$ genotyping:

541 Sense primer: 5'-GGTCTTGAAGACTGTCTGGTGTGAGA-3'

542 Antisense primer: 5′-CACAGGCCAGTTTAGGTCTTGCTAGG-3′

543

544 After genotyping, primary hippocampal neuron cultures were prepared from mutant and

545 corresponding control lines as described previously[12,60]. In brief, E16 hippocampi were

546 dissected, minced, treated with trypsin (Gibco) and DNase (SIGMA), and dissociated

547 mechanically into a cell suspension. Cells were resuspended in minimum essential

548 medium supplemented with B18 supplement, L-glutamine (Gibco), and 5% fetal calf

549 serum (Equitech-Bio), and plated onto glass-bottom dishes (MatTek, #1.5) precoated

550 with poly-L-lysine (SIGMA). Glial proliferation was prevented by adding 5 μM Ara-C

551 (SIGMA) 2 days after plating. For the comparison of spine nanostructure between wild-

552 type and mutant neurons, culture samples were processed for imaging at 18-22 DIV.

553 For pharmacological treatment, 10 μM CNQX or 20 μM bicuculline was applied to the

554 culture medium at 13 DIV and samples were processed for imaging at 19 DIV.

555

556 **Transfection and fluorescence labeling of primary hippocampal neurons**

557 Primary neurons were transfected with the indicated vectors using the calcium
558 phosphate precipitation method at 8–9 DIV according to a previously described
559 procedure[61]. All fluorescent proteins were expressed under the control of the β-actin
560 promoter.
561 The expression of the shRNA constructs was induced using the pSilencer vector
562 system. Briefly, the 19-nt target sequence and the reverse complement sequence of
563 the target were ligated into the shRNA expression vector separated by a 9-nt spacer
564 loop (TCTCTTGAA) (pSilencer 2.0-U6; Invitrogen). Stealth RNAi Negative Control
565 Duplexes (Invitrogen) were used as control shRNAs. The targeting sequences for
566 mouse Met, Arhgap15, and Ecrg4 are as follows:
567 Met RNAi sequence:
568 5'-GCAGTGAATTAGTTCGCTA-3
569 Arhgap15 RNAi sequence:
570 5'-AAGACAGATGTGAACATAC-3
571 Ecrg4 RNAi sequence:
572 5'- GAGGCTAAATTTGAAGAT-3'
573 The suppression of target protein expression by these transfected shRNAs was tested
574 by immunoblotting lysates of COS-7 cells co-transfected with a target gene construct
575 fused to a sequence encoding amino acids 98–106 of human influenza hemagglutinin
576 (HA), all under the control of the β-actin promoter. Overexpression of Cip4, Ecrg4, and
577 Npas4, genes upregulated in cultures derived from mouse models of schizophrenia,
578 was induced by transfection of plasmids containing the corresponding HA-fused cDNA
579 under the control of the β-actin promoter. Briefly, mouse Trip10 transcript variant 4
580 (Cip4; NM_001242391) and mouse Ecrg4 (NM_024283) were cloned, and an HA tag

581 was inserted into the C-terminus. Mouse Npas4 (NM_153553) was cloned according to
582 a previous report[62] and fused with a Flag-HA tag at its C-terminus. Human
583 neuropeptide Y (NPY) tagged with green fluorescent protein (GFP, a kind gift from Dr.
584 J. Takaska, NIH) was expressed under the control of the β-actin promoter.
585 For cell surface labeling of individual neurons in culture, cells were fixed and stained
586 with 1,1'-dioctadecyl-3,3,3',3'-tetramethylindocarbocyanine perchlorate (DiI; Molecular
587 Probes) as described previously[12].
588
589 **Immunocytochemistry**
590 Cultured hippocampal neurons expressing HA-tagged constructs were fixed with 2%
591 paraformaldehyde in PBS, permeabilized with 0.2% Triton X-100 in PBS, blocked with
592 5% normal goat serum, and reacted with rabbit anti-HA antibody (1:500; MBL) and
593 mouse anti-β-galactosidase antibody (1:500, SIGMA). After washing with PBS,
594 samples were reacted with Alexa Fluor 546-labeled goat anti-rabbit IgG antibody
595 (1:500; Invitrogen) and Alexa Fluor 647-labeled goat anti-mouse IgG antibody (1:500;
596 Invitrogen). For cell surface labeling with GFP, neurons expressing Ecrg4-HA-SEP
597 (superecliptic pHluorin) were reacted with anti-GFP VHH/nanobody conjugated to
598 Alexa Fluor 647 (1:4,000; Chromotek) in culture medium at 37°C.
599
600 **Structured illumination microscopy (SIM) imaging**
601 For 3D-SIM imaging, we used an inverted microscope (ECLIPSE Ti-E, NIKON)
602 equipped with an N-SIM-E system, 405, 488, 561, and 640 nm diode lasers (LU-NV,
603 NIKON), and an oil-immersion TIRF objective lens (SR Apo TIRF 100 ×, N.A. 1.49,
604 NIKON). All SIM images were acquired under strictly controlled conditions, including a

605 stage temperature of 28–29°C, to minimize the position and aberration fluctuations.
606 Spherical aberrations induced by refractive index mismatch were reduced by manually
607 adjusting the objective lens correction collar. Images were acquired using an EMCCD
608 camera (iXon3 DU-897E, Andor Technology) with 512 × 512 pixels (each pixel, 16 μm
609 square) operated in the read-out mode at 1 MHz with 16-bit analog-to-digital
610 conversion of the EM gain. All image-processing steps were performed in three
611 dimensions. The acquired image datasets were computationally reconstructed using
612 the reconstruction stack algorithm V2.10 of NIS-Elements AR (NIKON). An image stack
613 consisted of 63 axial (z) planes of 512 × 512 pixels in the x- and y-dimensions, with
614 pixel size of 32 × 32 nm. All 3D images were reconstructed in 120-nm z-steps spanning
615 7.56 μm in the z-axis. The voxel size fulfilled the Nyquist criterion requirements. Only
616 dendritic segments spatially isolated from other fluorescent objects were selected for
617 analysis because objects brighter than the targeted dendritic segments made image
618 thresholding unreliable. Quality checks of the acquired SIM images were performed as
619 described previously using the SIMcheck plugin for ImageJ[63].
620
621 **Spine isolation and shape measurement**
622 Spines were isolated by automated image thresholding using a previously described
623 method[12]. Briefly, the reconstructed SIM image stacks were first processed by
624 multilevel thresholding using the MATLAB built-in function [multithresh()] to produce
625 binary images, which were further processed by geodesic active contours using the
626 MATLAB built-in function [activecontour()]. The binary image stacks generated by
627 thresholding the SIM images were then processed for the automated detection of
628 spines. First, the dendritic shafts were fitted with elliptic cylinders and voxel clusters

outside the best-fit elliptic cylinders were identified as spine candidates. Next, the spine candidates were classified by their volumes and shapes. After selection, the junction between the dendritic shaft and spine was determined. Finally, the nanostructural parameters of isolated spines were measured. These steps are basically the same as those in our previous algorithm, but several points were improved, as described in the following sections (The original code for SIM image processing is available at https://shigeookabe.github.io/download-page-SIM/ with a password of “simspineimage”).

(1) Dendritic shaft fitting

We first estimated the shaft volume using the custom-made function "SIM_Fitdendrite" as previously described. In the new algorithm, the candidate spines were subsequently evaluated to determine whether their bases were large and spread on the shaft surface. If the spine base was large, the basal voxels were removed using the function "SIM_Removevoxel."

(2) Selection of the spines

Using the custom-made function "SIM_Position," spines with volumes too small, too elongated, or located at the image edge were removed as previously described. Small spine candidates with volumes less than twice the volume of a rectangular cuboid with edge lengths equal to the theoretical resolutions of SIM images (<0.01 μm^3) were rejected.

(3) Adjustment of the spine–shaft junction

We determined the location of spine–shaft junction using the custom-made function "SIM_Junction." This step was identical to our previous algorithm. Next, spines with

653 more than one connection site to the shaft were detected using the function
654 "SIM_Neck" and eliminated from further analysis.
655 (4) Measurement of nanostructural parameters
656 First, the angle of the spines was adjusted to be perpendicular to the long axis of the
657 dendritic shaft and within the xy-plane using the function "SIM_Angle." Next,
658 nanostructural parameters were measured using the function "SIM_Shape." In our
659 previous spine shape measurement study, a polygon mesh-based calculation was
660 performed. In the current study, we took a different approach using voxel-based
661 measurement. The calculation of structural parameters using voxel data was more
662 straightforward and required fewer calculation steps than the method based on polygon
663 mesh data. Spines were divided into 160-nm segments along the long axis using the
664 function "SIM_Shape." These spine segments were used to calculate the following 64
665 nanostructural parameters: spine length, surface area, base surface area, total volume,
666 volume of each spine segment (20 segments), convex hull volume of each spine
667 segment (20 segments), and convex hull ratio of each spine segment (20 segments).
668
669 **Analysis of the spine population data**
670 Differences in spine phenotype among model mice were analyzed at the population
671 level by PCA. We selected five parameters (spine length, base surface, total volume,
672 and volumes of the fifth and fifteenth spine segments) for the PCA-based dimensional
673 reduction. Two parameters that reflect the principal structural features (length and
674 volume) were first selected. Second, three other parameters that were mutually
675 independent and also independent from the first two parameters were chosen (pairwise

correlation coefficients < 0.3). The first three principal components (PC1–PC3) covered approximately 90% of the variance in the data.

The 2D presentation of spine population data using PC1 and PC2 reflected the overall pattern of the spine shape distribution, with thin, mushroom, and stubby spines separated in the feature space. Next, relative spine densities (number per area in the feature space) were mapped onto 80 × 80 square blocks spanning the standard deviation of ±4. Subsequently, two density plots, one derived from culture samples of disease model mice and the other from corresponding control mice, were subtracted to extract the differences in spine numbers with similar shape properties. The similarity between the two subtracted density plots was evaluated by calculating the 2D cross-correlation C using the following equation

$$C = \frac{\sum_{m=1}^{M}\sum_{n=1}^{N} X(m,n)Y(m,n)}{\sqrt{\sum_{m=1}^{M}\sum_{n=1}^{N} X(m,n)X(m,n)}\sqrt{\sum_{m=1}^{M}\sum_{n=1}^{N} Y(m,n)Y(m,n)}},$$

where X and Y correspond to the two subtracted density matrices. The 11 different subtracted density plots shown in Figure 2 were clustered using the MATLAB function "linkage," and the average distance between all pairs of elements in the two samples was calculated using the cluster algorithm.

Areas in the feature space enriched with mutant or control spines were then extracted by searching the 80 × 80 square blocks and identifying those where the difference in relative density was larger than the mean plus 3 × SD. Spine lengths, volumes, and axial profiles were then analyzed within areas enriched with either mutant or control spines.

700 **Time-lapse imaging of dendritic spines and image analysis**

701 Live cell 3D imaging was performed using an A1 confocal laser scanning microscope
702 (NIKON) equipped with 405, 488, 561, and 640 nm diode lasers (LU-NV, NIKON). Cells
703 at 15–18 DIV were maintained at 37°C under a continuous flow of 5% CO_2 to maintain
704 medium pH using a heater stage system (INUG2H-TIZSH, Tokai Hit) with a lid
705 designed for a glass-bottom dish to minimize evaporation. Horizontal and vertical drifts
706 were controlled by a motorized stage and a perfect focus system, respectively. Images
707 were acquired with an oil immersion objective lens (60×, NA) 1.4, NIKON) at a confocal
708 aperture of 1 AU. The imaged volume was 30.7 × 30.7 × 7.56 μm in x, y, and z
709 directions, respectively, and image stacks consisted of 17 planes separated by 500 nm.
710 Time-lapse images were recorded either at short intervals (15 min intervals for 24 h) or
711 long intervals (two time points separated by 24 h). Cultured neurons imaged at 24-h
712 interval were then fixed and immunostained with anti-HA to confirm the expression
713 levels of the transfected genes.

714 The image stacks obtained by time-lapse imaging were analyzed using custom-made
715 MATLAB scripts. First, 2D images were generated by maximal intensity projection of z-
716 stack images. These 2D images were processed to transform the outlines of dendritic
717 shafts to be aligned with straight lines. Spines were subsequently identified as objects
718 extending beyond the straight edges of the dendritic shafts. Identified spines were
719 segmented, and total fluorescence intensities were measured as a proxy for spine
720 volume. We classified the spines as stable (present throughout the imaging period),
721 newly formed (appearing within 24 h imaging period), and eliminated (lost within 24 h
722 imaging period). For newly formed and eliminated spines, we generated temporal
723 profiles of growth and shrinkage using the total fluorescence intensity values.

724

725 **RNA sequencing and gene expression analysis**

726 Total RNA was isolated from cultured hippocampal neurons at 19 DIV using the
727 RNeasy Mini Kit (QIAGEN) with the RNase-Free DNase Set (QIAGEN) according to
728 the manufacturer's protocols. The quality of the extracted RNA was initially assessed
729 using a NanoDrop spectrophotometer, and the RNA integrity number (RIN) score was
730 calculated for each sample using a Bioanalyzer (Agilent Technologies). The yields were
731 quantified using a Qubit Fluorometer (Thermo Fisher Scientific). Sequencing libraries
732 were prepared using the NEBNext Ultra Directional RNA Library Prep Kit for directional
733 libraries (New England BioLabs) and the KAPA HTP Library Preparation Kit (KAPA
734 Biosystems) according to the manufacturers' protocols. Paired-end RNA-seq libraries
735 were sequenced using the Illumina HiSeq and MGI DNBSEQ-G400 platforms. Three
736 independent culture preparations were used for RNA sequencing of each mouse model
737 and control library. Following quality control, the reads were aligned with the mouse
738 reference genome GRCm38/mm10 (GenBank assembly ID: GCA_000001635.2).
739 Expression levels of genes were analyzed based on the transcripts per million and
740 differential expression analysis was conducted using the DESeq2 package in R[64].
741 Differentially expressed genes (DEGs) were selected according to an adjusted $P <$
742 0.05 and a (log2)-fold change greater than 0.5.

743

744 **Simulation of spine development**

745 Spine growth was simulated using a dendrite model consisting of 1,000 segments,
746 each 0.25 μm in length (250 μm in total). The spine distribution was updated every 20
747 min over 10 days, covering the initial phase of spine development from 8 DIV to 17

748 DIV. The initial probability of new spine generation was set at 7.5×10^{-3} per segment
749 per hour and decreased thereafter in proportion to the accrued spine density increase
750 (by the final 24 h, the probability of spine generation [mean ± SD] was $3.2 \times 10^{-3} \pm 0.23$
751 $\times 10^{-3}$/segment/h). This probability function yielded an average of 1.2 ± 0.22 new
752 spines per 10 μm of dendrite every 24 h, in good agreement with the spine dynamics
753 measured by time-lapse imaging from 15–18 DIV (1.3 ± 0.63 new spines per 10 μm of
754 dendrite every 24 h). The model also set the increase in spine volume (V1) from $6.7 \times$
755 10^{-3} to 3.3×10^{-2} in 20 min. Spines in the early growth phase were treated as unstable,
756 with loss probability P1 ranging from 9.0×10^{-3} to 0.1 every 20 min. Spines were
757 modeled as stabilized when the individual volume reached a relative value of 1.0.
758 These stabilized spines then entered a shrinking phase with a probability P2 ranging
759 from 2.9×10^{-3} to 4.0×10^{-3} in 20 min. The shrinking rate V2 was set from 6.7×10^{-3} to
760 3.3×10^{-2} per 20 min. In simulations, the four parameters V1, V2, P1, and P2 were
761 varied within these indicated ranges to find the combination producing the best fit with
762 experimental data on the difference in spine lifetime distribution profile and turnover
763 rate at 24 h (the actual measurement interval). The simulation with the best-fit
764 parameters yielded a spine density comparable to measured data (0.57 ± 0.029 vs.
765 0.70 ± 0.17 spines
766 /μm of dendrite).
767
768 **Western blotting**
769 Total protein extracts from cultured hippocampal neurons were separated into cytosolic
770 and membrane fractions using Trident Membrane Protein Extraction Kit (GeneTex)
771 according to the manufacturer's protocol and separated on 10% sodium dodecyl sulfate

772 (SDS)-polyacrylamide gels or 15%–20% Tricine-SDS-polyacrylamide gels. The
773 separated proteins were then transferred onto nitrocellulose membranes (Millipore) or
774 PVDF membranes (Bio-Rad) using a wet transfer system. Membranes were blocked
775 with 5% bovine serum albumin in Tris-buffered saline plus Tween-20 (TBS-T, 20 mM
776 Tris-HCl, 137 mM NaCl, 0.2% Tween-20) for 1 h at room temperature, then incubated
777 overnight at 4°C with rabbit anti-Ecrg4 (1:1,000, SIGMA), rabbit anti-GluA1 (1:1,000,
778 Nittobo Medical), and mouse anti-α-tubulin (1:1,000, SIGMA) as indicated. The
779 membranes were washed and incubated with HRP-conjugated secondary antibody
780 against mouse or rabbit IgG (1:10,000, Amersham) for 2 h. Signals from the target
781 protein bands were detected using a SuperSignal™ West Atto detection kit (Pierce)
782 and imaged for quantitation (densitometry) using a ChemiDoc imaging system (Bio-
783 Rad).
784
785 **Statistics**
786 The statistical tests used for each experiment and the sample numbers (of neurons,
787 dendrites, or spines) are indicated in the corresponding figure legends. Statistical
788 significance was determined using the Wilcoxon rank sum test for two independent
789 samples (Figures 3, 5, and 8), two-way ANOVA for genotype and time (Figure 5), or
790 one-way ANOVA with post hoc Dunnett's tests between groups (Figure 7). Statistical
791 significance was set at $P < 0.05$.
792

Acknowledgments

We thank Toru Takumi for the 15q11-13$^{dup/+}$ mice, Katsuhiko Tabuchi for Nlgn3$^{R451C/(y\ or\ R451C)}$ mice, Yoko Yamagata for CaMKIIα$^{K42R/K42R}$ mice, and Justin Taraska for the NPY tagged with GFP. This work was supported by Grants-in-Aid for Scientific Research (20H00481, 20H05894, 20H05895 to S.O.), the Japan Agency for Medical Research and Development (JP19gm1310003 to S.O., T. N., and Y. G., JP22jm0210097 to S.O., JP19dm0207071 to A. A.), the Naito Foundation, and the Uehara Memorial Foundation.

Author contributions

Y.K. and S.O. conceived of the project and designed the methodology. Y.K. and Q.L. performed the experiments. R. S., A.A. and T.N. provided the animal resources and provided advice on analysis. Y.G. conducted the gene expression analysis. S.O. and Y.K. wrote the manuscript, with contributions from A.A., T.N., and Y.G.

Declarations of interests

The authors declare no competing interests. Additional affiliation of the authors is as follows; Shigeo Okabe; Director, RIKEN Center for Brain Science.

Declarations of generative AI and AI-assisted technologies in the writing process

The authors utilized Grammarly (https://app.grammarly.com/) for editing the text. The authors take full responsibility for the contents of the manuscript.

Resource availability

The original code for SIM image processing is available at
https://shigeookabe.github.io/download-page-SIM/
with a password of “simspineimage”.

References

1. Rochefort, N.L., and Konnerth, A. (2012). Dendritic spines: from structure to in vivo function. EMBO Rep *13*, 699–708. https://doi.org/10.1038/EMBOR.2012.102.
2. Sala, C., and Segal, M. (2014). Dendritic spines: the locus of structural and functional plasticity. Physiol Rev *94*, 141–188. https://doi.org/10.1152/physrev.00012.2013.
3. Matsuzaki, M., Ellis-Davies, G.C.R., Nemoto, T., Miyashita, Y., Iino, M., and Kasai, H. (2001). Dendritic spine geometry is critical for AMPA receptor expression in hippocampal CA1 pyramidal neurons. Nat Neurosci *4*, 1086–1092. https://doi.org/10.1038/NN736.
4. Matsuzaki, M., Honkura, N., Ellis-Davies, G.C.R., and Kasai, H. (2004). Structural basis of long-term potentiation in single dendritic spines. Nature *429*, 761–766. https://doi.org/10.1038/nature02617.
5. Nägerl, U.V., Eberhorn, N., Cambridge, S.B., and Bonhoeffer, T. (2004). Bidirectional activity-dependent morphological plasticity in hippocampal neurons. Neuron *44*, 759–767. https://doi.org/10.1016/j.neuron.2004.11.016.
6. Zhou, Q., Homma, K.J., and Poo, M.M. (2004). Shrinkage of dendritic spines associated with long-term depression of hippocampal synapses. Neuron *44*, 749–757. https://doi.org/10.1016/j.neuron.2004.11.011.
7. Loewenstein, Y., Kuras, A., and Rumpel, S. (2011). Multiplicative dynamics underlie the emergence of the log-normal distribution of spine sizes in the neocortex in vivo. Journal of Neuroscience *31*, 9481–9488. https://doi.org/10.1523/JNEUROSCI.6130-10.2011.
8. Loewenstein, Y., Yanover, U., and Rumpel, S. (2015). Predicting the dynamics of network connectivity in the neocortex. Journal of Neuroscience *35*, 12535–12544. https://doi.org/10.1523/JNEUROSCI.2917-14.2015.
9. Statman, A., Kaufman, M., Minerbi, A., Ziv, N.E., and Brenner, N. (2014). Synaptic size dynamics as an effectively stochastic process. PLoS Comput Biol *10*. https://doi.org/10.1371/JOURNAL.PCBI.1003846.
10. Hazan, L., and Ziv, N.E. (2020). Activity dependent and independent determinants of synaptic size diversity. J Neurosci *40*, 2828–2848. https://doi.org/10.1523/JNEUROSCI.2181-19.2020.
11. Tønnesen, J., Katona, G., Rózsa, B., and Nägerl, U.V. (2014). Spine neck plasticity regulates compartmentalization of synapses. Nat Neurosci *17*, 678–685. https://doi.org/10.1038/nn.3682.

12. Kashiwagi, Y., Higashi, T., Obashi, K., Sato, Y., Komiyama, N.H., Grant, S.G.N., and Okabe, S. (2019). Computational geometry analysis of dendritic spines by structured illumination microscopy. Nat Commun *10*, 1285. https://doi.org/10.1038/s41467-019-09337-0.
13. Zaccard, C.R., Shapiro, L., Martin-de-Saavedra, M.D., Pratt, C., Myczek, K., Song, A., Forrest, M.P., and Penzes, P. (2020). Rapid 3D enhanced resolution microscopy reveals diversity in dendritic spinule dynamics, regulation, and function. Neuron *107*, 522–537. https://doi.org/10.1016/j.neuron.2020.04.025.
14. Penzes, P., Cahill, M.E., Jones, K.A., VanLeeuwen, J.-E., and Woolfrey, K.M. (2011). Dendritic spine pathology in neuropsychiatric disorders. Nat Neurosci *14*, 285–293. https://doi.org/10.1038/nn.2741.
15. Fromer, M., Pocklington, A.J., Kavanagh, D.H., Williams, H.J., Dwyer, S., Gormley, P., Georgieva, L., Rees, E., Palta, P., Ruderfer, D.M., et al. (2014). De novo mutations in schizophrenia implicate synaptic networks. Nature *506*, 179–184. https://doi.org/10.1038/NATURE12929.
16. Rodriguez-Murillo, L., Gogos, J.A., and Karayiorgou, M. (2012). The genetic architecture of schizophrenia: new mutations and emerging paradigms. Annu Rev Med *63*, 63–80. https://doi.org/10.1146/ANNUREV-MED-072010-091100.
17. Gulsuner, S., Walsh, T., Watts, A.C., Lee, M.K., Thornton, A.M., Casadei, S., Rippey, C., Shahin, H., Nimgaonkar, V.L., Go, R.C.P., et al. (2013). Spatial and temporal mapping of de novo mutations in schizophrenia to a fetal prefrontal cortical network. Cell *154*, 518–529. https://doi.org/10.1016/J.CELL.2013.06.049.
18. Bourgeron, T. (2015). From the genetic architecture to synaptic plasticity in autism spectrum disorder. Nat Rev Neurosci *16*, 551–563. https://doi.org/10.1038/NRN3992.
19. Terashima, H., Minatohara, K., Maruoka, H., and Okabe, S. (2022). Imaging neural circuit pathology of autism spectrum disorders: autism-associated genes, animal models and the application of in vivo two-photon imaging. Microscopy (Oxf) *71*, I81–I99. https://doi.org/10.1093/JMICRO/DFAB039.
20. Zieger, H.L., and Choquet, D. (2021). Nanoscale synapse organization and dysfunction in neurodevelopmental disorders. Neurobiol Dis *158*, 105453. https://doi.org/10.1016/J.NBD.2021.105453.
21. Yilmaz, M., Yalcin, E., Presumey, J., Aw, E., Ma, M., Whelan, C.W., Stevens, B., McCarroll, S.A., and Carroll, M.C. (2021). Overexpression of schizophrenia susceptibility factor human complement C4A promotes excessive synaptic loss

and behavioral changes in mice. Nat Neurosci *24*, 214–224. https://doi.org/10.1038/S41593-020-00763-8.

22. Obi-Nagata, K., Suzuki, N., Miyake, R., MacDonald, M.L., Fish, K.N., Ozawa, K., Nagahama, K., Okimura, T., Tanaka, S., Kano, M., et al. (2023). Distorted neurocomputation by a small number of extra-large spines in psychiatric disorders. Sci Adv *9*, eade5973. https://doi.org/10.1126/SCIADV.ADE5973.

23. Mukai, J., Dhilla, A., Drew, L.J., Stark, K.L., Cao, L., MacDermott, A.B., Karayiorgou, M., and Gogos, J.A. (2008). Palmitoylation-dependent neurodevelopmental deficits in a mouse model of 22q11 microdeletion. Nat Neurosci *11*, 1302–1310. https://doi.org/10.1038/nn.2204.

24. Nakai, N., Takumi, T., Nakai, J., and Sato, M. (2018). Common defects of spine dynamics and circuit function in neurodevelopmental disorders: A systematic review of findings from in vivo optical imaging of mouse models. Front Neurosci *12*. https://doi.org/10.3389/FNINS.2018.00412/PDF.

25. Shcheglovitov, A., Shcheglovitova, O., Yazawa, M., Portmann, T., Shu, R., Sebastiano, V., Krawisz, A., Froehlich, W., Bernstein, J.A., Hallmayer, J.F., et al. (2013). SHANK3 and IGF1 restore synaptic deficits in neurons from 22q13 deletion syndrome patients. Nature *503*, 267–271. https://doi.org/10.1038/NATURE12618.

26. Llamosas, N., Arora, V., Vij, R., Kilinc, M., Bijoch, L., Rojas, C., Reich, A., Sridharan, B.P., Willems, E., Piper, D.R., et al. (2020). SYNGAP1 controls the maturation of dendrites, synaptic function, and network activity in developing human neurons. J Neurosci *40*, 7980–7994. https://doi.org/10.1523/JNEUROSCI.1367-20.2020.

27. Yamamoto, K., Kuriu, T., Matsumura, K., Nagayasu, K., Tsurusaki, Y., Miyake, N., Yamamori, H., Yasuda, Y., Fujimoto, M., Fujiwara, M., et al. (2021). Multiple alterations in glutamatergic transmission and dopamine D2 receptor splicing in induced pluripotent stem cell-derived neurons from patients with familial schizophrenia. Transl Psychiatry *11*, 548. https://doi.org/10.1038/S41398-021-01676-1.

28. Wen, Z., Nguyen, H.N., Guo, Z., Lalli, M.A., Wang, X., Su, Y., Kim, N.S., Yoon, K.J., Shin, J., Zhang, C., et al. (2014). Synaptic dysregulation in a human iPS cell model of mental disorders. Nature *515*, 414–418. https://doi.org/10.1038/NATURE13716.

29. Chisholm, K., Lin, A., Abu-Akel, A., and Wood, S.J. (2015). The association between autism and schizophrenia spectrum disorders: A review of eight

alternate models of co-occurrence. Neurosci Biobehav Rev *55*, 173–183. https://doi.org/10.1016/J.NEUBIOREV.2015.04.012.

30. De Crescenzo, F., Postorino, V., Siracusano, M., Riccioni, A., Armando, M., Curatolo, P., and Mazzone, L. (2019). Autistic symptoms in schizophrenia spectrum disorders: A systematic review and meta-analysis. Front Psychiatry *10*. https://doi.org/10.3389/FPSYT.2019.00078/PDF.

31. Nenadić, I., Meller, T., Evermann, U., Schmitt, S., Pfarr, J.K., Abu-Akel, A., and Grezellschak, S. (2021). Subclinical schizotypal vs. autistic traits show overlapping and diametrically opposed facets in a non-clinical population. Schizophr Res *231*, 32–41. https://doi.org/10.1016/J.SCHRES.2021.02.018.

32. Crespi, B., and Badcock, C. (2008). Psychosis and autism as diametrical disorders of the social brain. Behav Brain Sci *31*, 241–261. https://doi.org/10.1017/S0140525X08004214.

33. Pratt, J., Winchester, C., Dawson, N., and Morris, B. (2012). Advancing schizophrenia drug discovery: optimizing rodent models to bridge the translational gap. Nat Rev Drug Discov *11*, 560–570. https://doi.org/10.1038/NRD3649.

34. Isshiki, M., Tanaka, S., Kuriu, T., Tabuchi, K., Takumi, T., and Okabe, S. (2014). Enhanced synapse remodelling as a common phenotype in mouse models of autism. Nat Commun *5*, 4742. https://doi.org/10.1038/ncomms5742.

35. Lee, E., Lee, J., and Kim, E. (2017). Excitation/inhibition imbalance in animal models of autism spectrum disorders. Biol Psychiatry *81*, 838–847. https://doi.org/10.1016/J.BIOPSYCH.2016.05.011.

36. Tabuchi, K., Blundell, J., Etherton, M.R., Hammer, R.E., Liu, X., Powell, C.M., and Südhof, T.C. (2007). A neuroligin-3 mutation implicated in autism increases inhibitory synaptic transmission in mice. Science *318*, 71–76. https://doi.org/10.1126/science.1146221.

37. Etherton, M., Földy, C., Sharma, M., Tabuchi, K., Liu, X., Shamloo, M., Malenka, R.C., and Südhof, T.C. (2011). Autism-linked neuroligin-3 R451C mutation differentially alters hippocampal and cortical synaptic function. Proc Natl Acad Sci U S A *108*, 13764–13769. https://doi.org/10.1073/pnas.1111093108.

38. Komiyama, N.H., Watabe, A.M., Carlisle, H.J., Porter, K., Charlesworth, P., Monti, J., Strathdee, D.J.C., O'Carroll, C.M., Martin, S.J., Morris, R.G.M., et al. (2002). SynGAP regulates ERK/MAPK signaling, synaptic plasticity, and learning in the complex with postsynaptic density 95 and NMDA receptor. The Journal of Neuroscience *22*, 9721–9732. https://doi.org/22/22/9721 [pii].

39. Matsumura, K., Seiriki, K., Okada, S., Nagase, M., Ayabe, S., Yamada, I., Furuse, T., Shibuya, H., Yasuda, Y., Yamamori, H., et al. (2020). Pathogenic POGZ mutation causes impaired cortical development and reversible autism-like phenotypes. Nat Commun *11*, 859. https://doi.org/10.1038/s41467-020-14697-z.
40. Nakatani, J., Tamada, K., Hatanaka, F., Ise, S., Ohta, H., Inoue, K., Tomonaga, S., Watanabe, Y., Chung, Y.J., Banerjee, R., et al. (2009). Abnormal behavior in a chromosome- engineered mouse model for human 15q11-13 duplication seen in autism. Cell *137*, 1235–1246. https://doi.org/10.1016/j.cell.2009.04.024.
41. Baba, M., Yokoyama, K., Seiriki, K., Naka, Y., Matsumura, K., Kondo, M., Yamamoto, K., Hayashida, M., Kasai, A., Ago, Y., et al. (2019). Psychiatric-disorder-related behavioral phenotypes and cortical hyperactivity in a mouse model of 3q29 deletion syndrome. Neuropsychopharmacology *44*, 2125–2135. https://doi.org/10.1038/s41386-019-0441-5.
42. Saito, R., Miyoshi, C., Koebis, M., Kushima, I., Nakao, K., Mori, D., Ozaki, N., Funato, H., Yanagisawa, M., and Aiba, A. (2021). Two novel mouse models mimicking minor deletions in 22q11.2 deletion syndrome revealed the contribution of each deleted region to psychiatric disorders. Mol Brain *14*. https://doi.org/10.1186/S13041-021-00778-7.
43. Nagahama, K., Sakoori, K., Watanabe, T., Kishi, Y., Kawaji, K., Koebis, M., Nakao, K., Gotoh, Y., Aiba, A., Uesaka, N., et al. (2020). Setd1a insufficiency in mice attenuates excitatory synaptic function and recapitulates schizophrenia-related behavioral abnormalities. Cell Rep *32*, 108126. https://doi.org/10.1016/J.CELREP.2020.108126.
44. Yamagata, Y., Kobayashi, S., Umeda, T., Inoue, A., Sakagami, H., Fukaya, M., Watanabe, M., Hatanaka, N., Totsuka, M., Yagi, T., et al. (2009). Kinase-dead knock-in mouse reveals an essential role of kinase activity of Ca^{2+}/calmodulin-dependent protein kinase IIα in dendritic spine enlargement, long-term potentiation, and learning. Journal of Neuroscience *29*, 7607–7618. https://doi.org/10.1523/JNEUROSCI.0707-09.2009.
45. Yamasaki, N., Maekawa, M., Kobayashi, K., Kajii, Y., Maeda, J., Soma, M., Takao, K., Tanda, K., Ohira, K., Toyama, K., et al. (2008). Alpha-CaMKII deficiency causes immature dentate gyrus, a novel candidate endophenotype of psychiatric disorders. Mol Brain *1*, 6. https://doi.org/10.1186/1756-6606-1-6.
46. Featherstone, R.E., Shimada, T., Crown, L.M., Melnychenko, O., Yi, J., Matsumoto, M., Tajinda, K., Mihara, T., Adachi, M., and Siegel, S.J. (2022). Calcium/calmodulin-dependent protein kinase IIα heterozygous knockout mice

997 show electroencephalogram and behavioral changes characteristic of a
998 subpopulation of schizophrenia and intellectual impairment. Neuroscience *499*,
999 104–117. https://doi.org/10.1016/J.NEUROSCIENCE.2022.07.023.
1000 47. Qiu, S., Lu, Z., and Levitt, P. (2014). MET receptor tyrosine kinase controls
1001 dendritic complexity, spine morphogenesis, and glutamatergic synapse
1002 maturation in the hippocampus. J Neurosci *34*, 16166–16179.
1003 https://doi.org/10.1523/JNEUROSCI.2580-14.2014.
1004 48. Bloodgood, B.L., Sharma, N., Browne, H.A., Trepman, A.Z., and Greenberg,
1005 M.E. (2013). The activity-dependent transcription factor NPAS4 regulates
1006 domain-specific inhibition. Nature *503*, 121–125.
1007 https://doi.org/10.1038/nature12743.
1008 49. Spiegel, I., Mardinly, A.R., Gabel, H.W., Bazinet, J.E., Couch, C.H., Tzeng, C.P.,
1009 Harmin, D.A., and Greenberg, M.E. (2014). Npas4 regulates excitatory-inhibitory
1010 balance within neural circuits through cell-type-specific gene programs. Cell *157*,
1011 1216–1229. https://doi.org/10.1016/J.CELL.2014.03.058.
1012 50. Zamboni, V., Armentano, M., Saró, G., Ciraolo, E., Ghigo, A., Germena, G.,
1013 Umbach, A., Valnegri, P., Passafaro, M., Carabelli, V., et al. (2016). Disruption of
1014 ArhGAP15 results in hyperactive Rac1, affects the architecture and function of
1015 hippocampal inhibitory neurons and causes cognitive deficits. Sci Rep *6*.
1016 https://doi.org/10.1038/SREP34877.
1017 51. Ba, W., Selten, M.M., van der Raadt, J., van Veen, H., Li, L.L., Benevento, M.,
1018 Oudakker, A.R., Lasabuda, R.S.E., Letteboer, S.J., Roepman, R., et al. (2016).
1019 ARHGAP12 functions as a developmental brake on excitatory synapse function.
1020 Cell Rep *14*, 1355–1368. https://doi.org/10.1016/J.CELREP.2016.01.037.
1021 52. Nakatani, Y., Kiyonari, H., and Kondo, T. (2019). Ecrg4 deficiency extends the
1022 replicative capacity of neural stem cells in a Foxg1-dependent manner.
1023 Development *146*, dev168120. https://doi.org/10.1242/DEV.168120.
1024 53. Richter, M., Lalli, E., and Ruggiero, C. (2023). Complex and pleiotropic signaling
1025 pathways regulated by the secreted protein augurin. Cell Commun Signal *21*, 69.
1026 https://doi.org/10.1186/S12964-023-01090-8.
1027 54. MacDonald, M.L., Alhassan, J., Newman, J.T., Richard, M., Gu, H., Kelly, R.M.,
1028 Sampson, A.R., Fish, K.N., Penzes, P., Wills, Z.P., et al. (2017). Selective loss of
1029 smaller spines in Schizophrenia. American Journal of Psychiatry *174*, 586–594.
1030 https://doi.org/10.1176/APPI.AJP.2017.16070814/SUPPL_FILE/APPI.AJP.2017.
1031 16070814.DS001.PDF.
1032 55. Pfeiffer, T., Poll, S., Bancelin, S., Angibaud, J., Inavalli, V.K., Keppler, K., Mittag,

1033 M., Fuhrmann, M., and Nägerl, U.V. (2018). Chronic 2P-STED imaging reveals
1034 high turnover of dendritic spines in the hippocampus in vivo. Elife *7*.
1035 https://doi.org/10.7554/eLife.34700.
1036 56. Attardo, A., Fitzgerald, J.E., and Schnitzer, M.J. (2015). Impermanence of
1037 dendritic spines in live adult CA1 hippocampus. Nature *523*, 592–596.
1038 https://doi.org/10.1038/nature14467.
1039 57. Moriguchi, T., Takeda, S., Iwashita, S., Enomoto, K., Sawamura, T., Koshimizu,
1040 U., and Kondo, T. (2018). Ecrg4 peptide is the ligand of multiple scavenger
1041 receptors. Sci Rep *8*. https://doi.org/10.1038/S41598-018-22440-4.
1042 58. Stewart, L.R., Hall, A.L., Kang, S.H.L., Shaw, C.A., and Beaudet, A.L. (2011).
1043 High frequency of known copy number abnormalities and maternal duplication
1044 15q11-q13 in patients with combined schizophrenia and epilepsy. BMC Med
1045 Genet *12*, 1–10. https://doi.org/10.1186/1471-2350-12-154/TABLES/4.
1046 59. Ingason, A., Kirov, G., Giegling, I., Hansen, T., Isles, A.R., Jakobsen, K.D.,
1047 Kristinsson, K.T., Le Roux, L., Gustafsson, O., Craddock, N., et al. (2011).
1048 Maternally derived microduplications at 15q11-q13: implication of imprinted
1049 genes in psychotic illness. Am J Psychiatry *168*, 408–417.
1050 https://doi.org/10.1176/APPI.AJP.2010.09111660.
1051 60. Okabe, S., Kim, H.D., Miwa, A., Kuriu, T., and Okado, H. (1999). Continual
1052 remodeling of postsynaptic density and its regulation by synaptic activity. Nat
1053 Neurosci *2*, 804–811. https://doi.org/10.1038/12175.
1054 61. Shin, E., Kashiwagi, Y., Kuriu, T., Iwasaki, H., Tanaka, T., Koizumi, H., Gleeson,
1055 J.G., and Okabe, S. (2013). Doublecortin-like kinase enhances dendritic
1056 remodelling and negatively regulates synapse maturation. Nat Commun *4*, 1440.
1057 https://doi.org/10.1038/ncomms2443.
1058 62. Ooe, N., Saito, K., Mikami, N., Nakatuka, I., and Kaneko, H. (2004). Identification
1059 of a novel basic helix-loop-helix-PAS factor, NXF, reveals a Sim2 competitive,
1060 positive regulatory role in dendritic-cytoskeleton modulator drebrin gene
1061 expression. Mol Cell Biol *24*, 608–616. https://doi.org/10.1128/MCB.24.2.608-
1062 616.2004.
1063 63. Ball, G., Demmerle, J., Kaufmann, R., Davis, I., Dobbie, I.M., and Schermelleh,
1064 L. (2015). SIMcheck: a toolbox for successful super-resolution structured
1065 illumination microscopy. Sci Rep *5*, 15915. https://doi.org/10.1038/srep15915.
1066 64. Love, M.I., Huber, W., and Anders, S. (2014). Moderated estimation of fold
1067 change and dispersion for RNA-seq data with DESeq2. Genome Biol *15*.
1068 https://doi.org/10.1186/S13059-014-0550-8.

1069

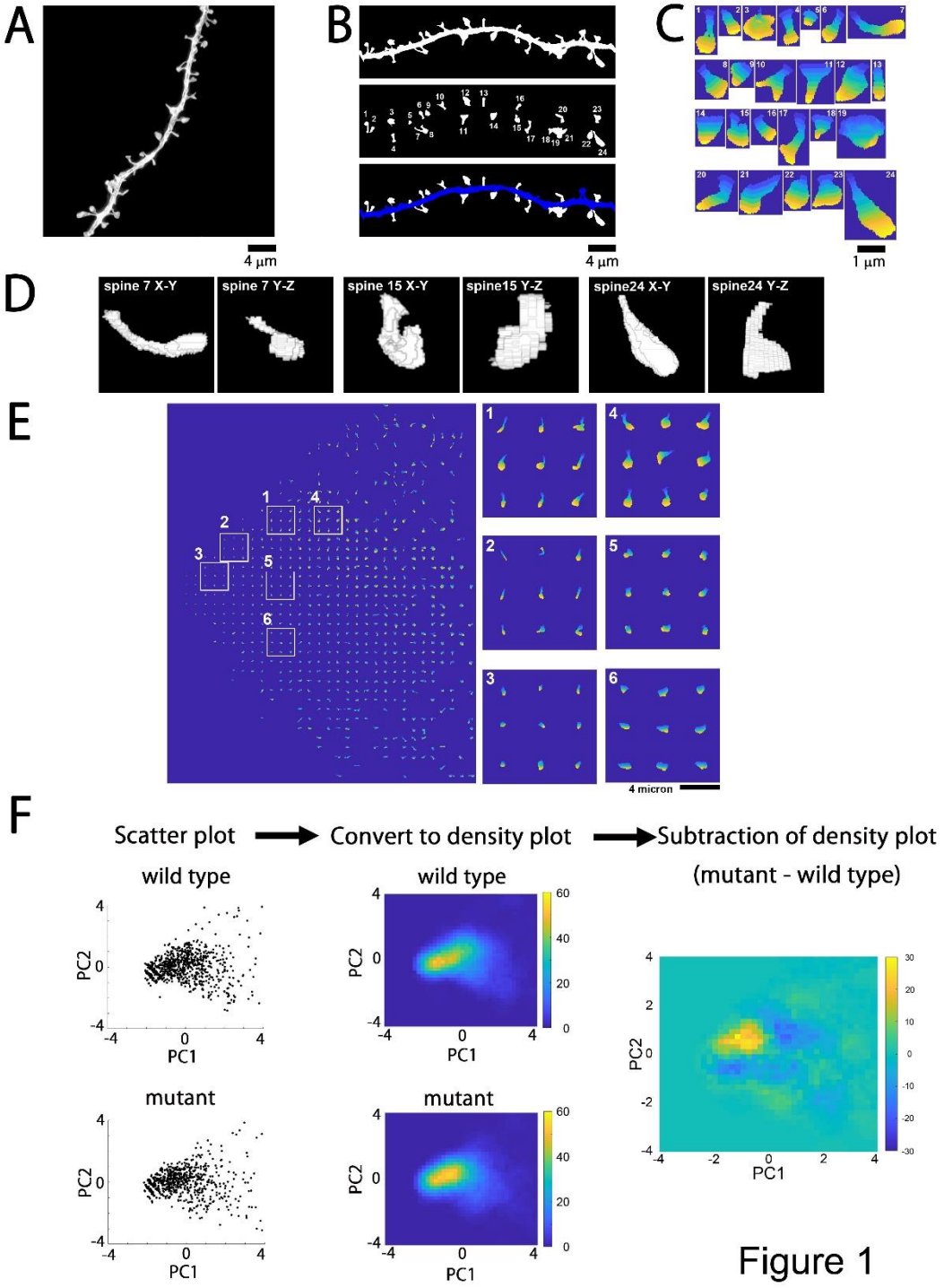

Figure 1

1070

1071

1072 **Figure 1**

1073 SIM imaging of dendritic spines, automated measurements of spine morphology, and
1074 generation of subtracted spine density plots for population-level analysis. (A) Original
1075 SIM image of a dendritic shaft stained with lipophilic membrane dye DiI. (B) Binarized
1076 image of the same dendrite (top) and segmented spines numbered from 1 to 24
1077 (middle). The bottom image shows segmented spines (white) and the dendritic shaft
1078 (blue). (C) Enlarged images of the individual spines shown in (B). The pseudocolor
1079 images indicating the relative positions of the spine segments from the base (blue) to
1080 the tip (yellow). (D) 3D views of three spines (No. 7, 15, and 24) viewed from different
1081 angles. (E) Principal component analysis (PCA)-based dimensional reduction of spine
1082 characteristics plotted in the plane of principal component (PC)1 and PC2. (F) Process
1083 of generating a subtracted density plot. The scatter plot of spine distribution in the
1084 PC1–PC2 plane based on morphological parameters was converted into a density plot
1085 for each culture source (genotype or treatment group), and the corresponding plots
1086 were subtracted to reveal differences in spine morphology at the population level. Bars,
1087 4 μm for A, B, and E, 1 μm for C.
1088

1089

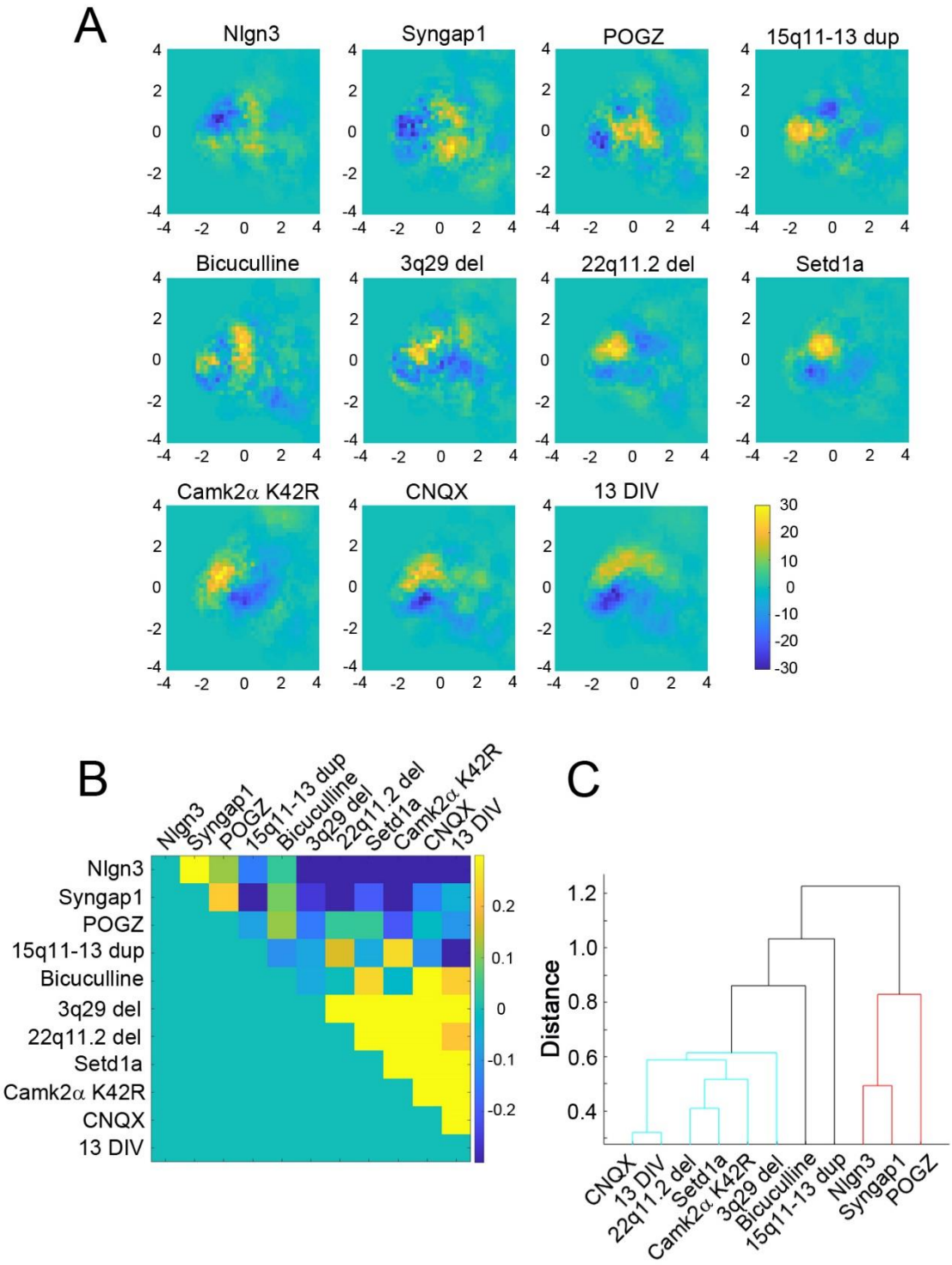
A
Nlgn3
Syngap1
POGZ
15q11-13 dup
Bicuculline
3q29 del
22q11.2 del
Setd1a
Camk2α K42R
CNQX
13 DIV
B
C
Distance
Figure 2

1090

1091

1092 **Figure 2**

1093 Spine population profiles for each model and corresponding control mouse line
1094 presented as subtracted density plots. (A) The subtracted density plots for eight
1095 disease mouse models (Nlgn3$^{R451C/(y\ or\ R451C)}$, Syngap1$^{+/-}$, POGZ$^{Q1038R/+}$, 15q11-13$^{dup/+}$,
1096 3q29$^{del/+}$, 22q11.2$^{del/+}$, Setd1a$^{+/-}$, and CaMKIIα$^{K42R/K42R}$) and three different culture
1097 conditions (immature culture at 13 DIV, AMPA glutamate receptor blocker CNQX
1098 treatment, and $GABA_A$ receptor blocker bicuculine treatment). The areas with a higher
1099 density of spines from mutant disease model mice are shown in yellow, and the areas
1100 with reduced density are shown in blue. The total number of spines (first number, n)
1101 analyzed from control and mutant mouse neurons and the corresponding number of
1102 dendrites (number in parentheses) are as follows: Nlgn3$^{R451C/(y\ or\ R451C)}$; n = 1,134 (58)
1103 and 1,204 (59), Syngap1$^{+/-}$; n = 991 (65) and 1,371 (83), POGZ$^{Q1038R/+}$; n = 1,341 (72)
1104 and 1,271 (72), 15q11-13$^{dup/+}$; n = 1, 208 (68) and 1,099 (63), 3q29$^{del/+}$; n = 1,429 (66)
1105 and 1,408 (66), 22q11.2$^{del/+}$; n = 1,143 (66) and 914 (63), Setd1a$^{+/-}$; n = 1,381 (71) and
1106 1,405 (71), CaMKIIα$^{K42R/K42R}$; n = 880 (58) and 763 (54). All data are from three
1107 independent culture preparations. (B) Matrix of the 2D cross-correlations among
1108 subtracted density plots. In the lower right area, a spine group showing similar
1109 morphological changes can be identified. This group corresponded to the mouse
1110 models of schizophrenia. (C) Unbiased clustering of spine samples showing two
1111 distinct groups corresponding to schizophrenia (cyan) and ASD (red).

1112

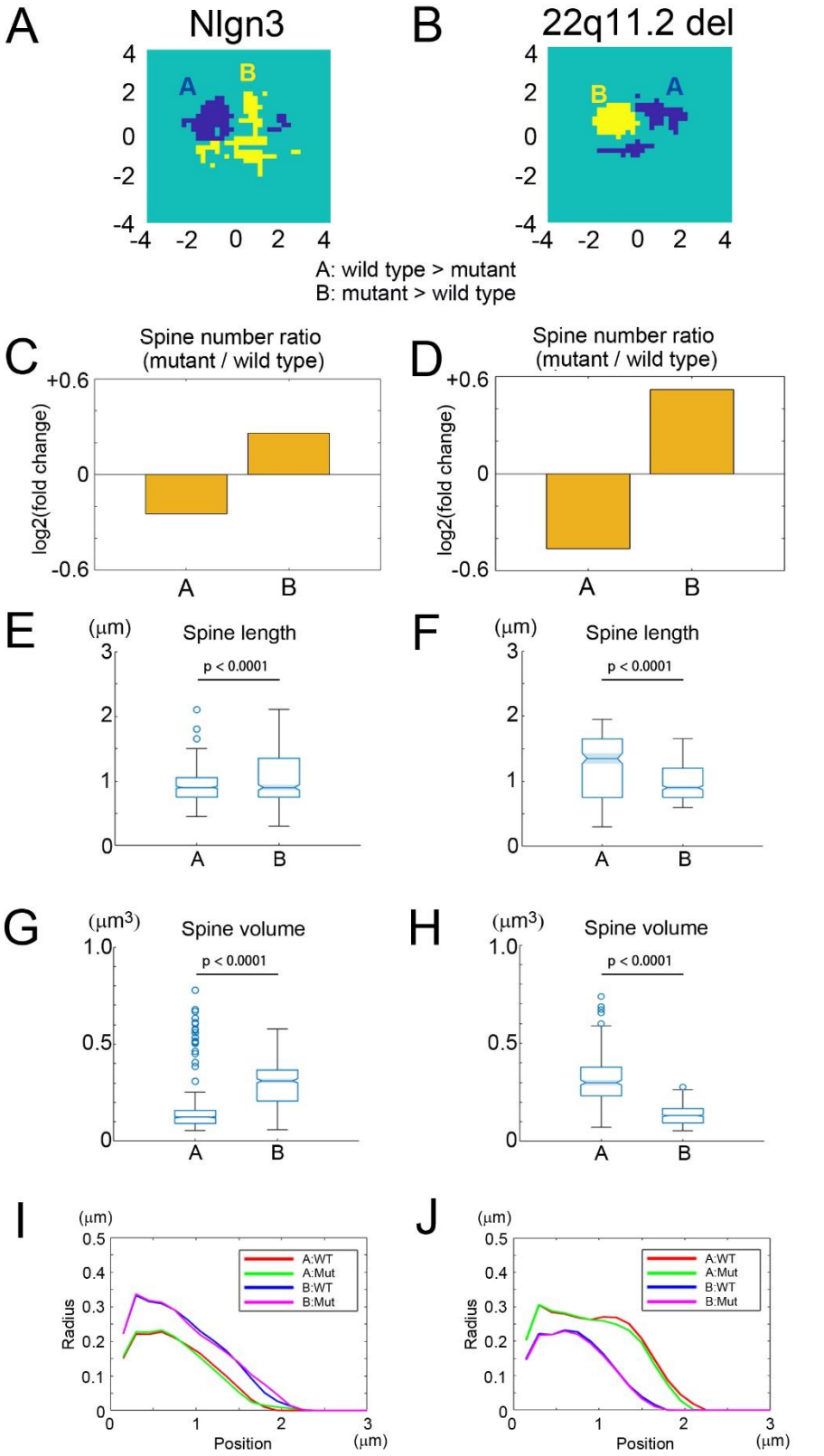

Figure 3

1113

1114

1115 **Figure 3**

1116 Distinct morphological properties of spines in cultured neurons derived from
1117 schizophrenia model mice compared with ASD model mice. (A and B) Areas with large
1118 differences (> 3 × SD) between control and mutant mice in terms of spine number per
1119 area in the feature space. The areas either enriched in the control (area A, blue region)
1120 or mutant (area B, yellow region) are shown. The positions of A and B are reversed
1121 between Nlgn3$^{R451C/(y\ or\ R451C)}$ and 22q11.2$^{del/+}$. The total numbers of spines (n) in areas
1122 A and B were as follows: Nlgn3$^{R451C/(y\ or\ R451C)}$, control in A = 409, mutant in A = 366,
1123 control in B = 226, and mutant in B = 287; 22q11.2$^{del/+}$, control in A = 195, mutant in A =
1124 113, control in B = 268, and mutant in B = 307. Subtraction of spine numbers per area
1125 was performed after normalization by total spine numbers (Nlgn3$^{R451C/(y\ or\ R451C)}$, control
1126 = 1134 and mutant = 1204; 22q11.2$^{del/+}$, control = 1143 and mutant = 914). (C and D)
1127 The relative number of spines distributed in areas A and B. (E and F) Distributions of
1128 spine lengths within the areas A and B. The Nlgn3$^{R451C/(y\ or\ R451C)}$ mouse model of ASD
1129 was enriched in longer spines, whereas the 22q11.2$^{del/+}$ mouse model of schizophrenia
1130 was enriched in shorter spines. (G and H) Spine volumes within areas A and B. The
1131 Nlgn3$^{R451C/(y\ or\ R451C)}$ mouse model was enriched in large spines, while the 22q11.2$^{del/+}$
1132 mouse model was enriched in small spines. (I and J) The profiles of spines along their
1133 long axes. The trend observed for spine length and diameter was reversed between
1134 Nlgn3$^{R451C/(y\ or\ R451C)}$ and 22q11.2$^{del/+}$ mouse models. Statistical significance was
1135 determined using the Wilcoxon rank sum test (Nlgn3$^{R451C/(y\ or\ R451C)}$, n = 775 in area A
1136 and n = 513 in area B; 22q11.2$^{del/+}$, n = 308 in area A and n = 575 in area B).
1137

1138

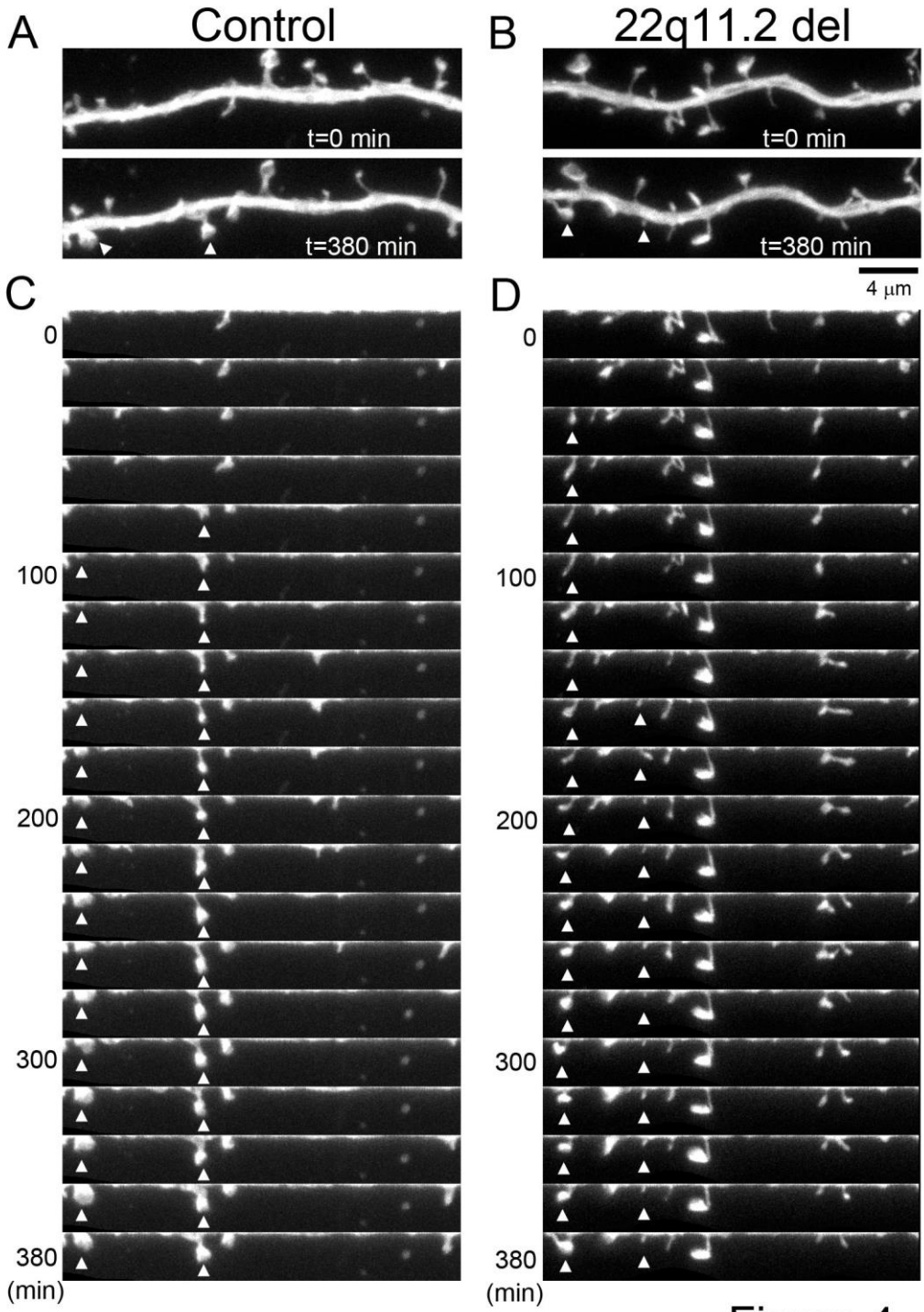

Figure 4

1139

1140

1141

1142 **Figure 4**

1143 Time-lapse imaging of neurons derived from 22q11.2$^{del/+}$ schizophrenia model mice and

1144 corresponding control mice. (A and B) Images of dendritic segments from control

1145 neurons (A) and 22q11.2$^{del/+}$ neurons (B) at two different times points. (C and D)

1146 Montages of time-lapse images from control neurons (C) and 22q11.2$^{del/+}$ neurons (D).

1147 The curved dendrites were straightened, revealing newly formed spines (arrowheads)

1148 as fluorescent objects appearing at the edge of the dendritic shafts. Bar, 4 μm.

1149

1150

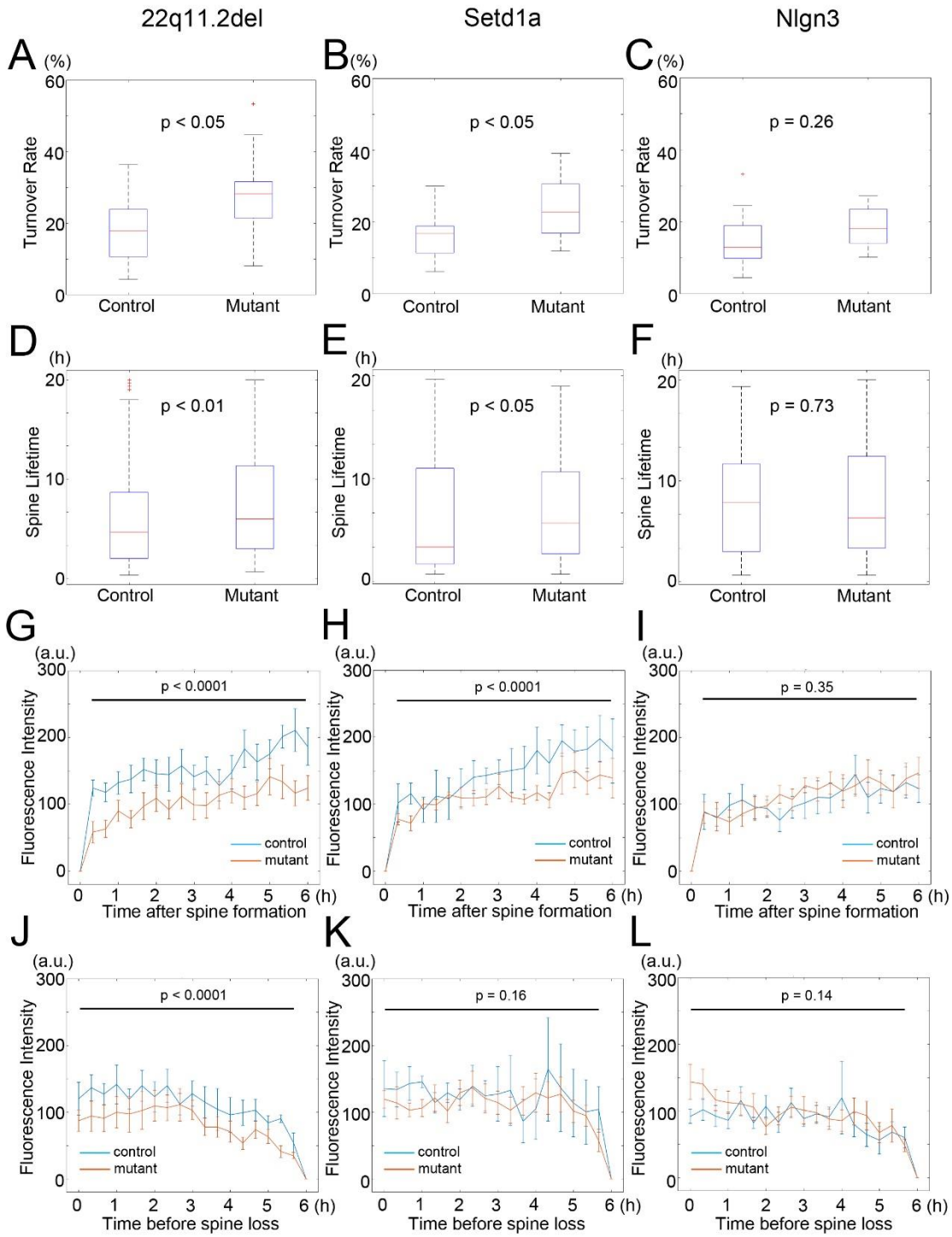
22q11.2del
Setd1a
Nlgn3
A
B
C
(%)
Turnover Rate
p < 0.05
p < 0.05
p = 0.26
Control
Mutant
D
E
F
(h)
Spine Lifetime
p < 0.01
p < 0.05
p = 0.73
G
H
I
(a.u.)
Fluorescence Intensity
p < 0.0001
p < 0.0001
p = 0.35
control
mutant
Time after spine formation
J
K
L
p < 0.0001
p = 0.16
p = 0.14
Time before spine loss

Figure 5

1154 **Figure 5**

1155 Turnover rate, lifetime, and growth/shrinkage profiles of dendritic spines in cultured
1156 neurons derived from 22q11.2$^{del/+}$, Setd1a$^{+/-}$, and Nlgn3$^{R451C/(y\ or\ R451C)}$ mice as well as
1157 the corresponding controls. (A-C) Spine turnover rates in the three mutant mouse
1158 models compared to the controls (n = 16 dendrites from control neurons and 11
1159 dendrites from 22q11.2$^{del/+}$ neurons, n = 10 control and n = 14 Setd1a$^{+/-}$ dendrites, n =
1160 8 control and n = 8 Nlgn3$^{R451C/(y\ or\ R451C)}$ dendrites). (D-F) Spine lifetimes for the three
1161 mutant mouse models compared with corresponding controls. (n = 186 (11) control and
1162 n = 166 (7) 22q11.2$^{del/+}$ spines (neurons), n = 82 (5) control and n = 202 (8) Setd1a$^{+/-}$
1163 spines (neurons), n = 98 (8) control and n = 125 (8) Nlgn3$^{R451C/(y\ or\ R451C)}$ spines
1164 (neurons)). (G-I) Temporal patterns of spine growth (n = 11 control and n = 7
1165 22q11.2$^{del/+}$ neurons, n = 5 control and n = 8 Setd1a$^{+/-}$ neurons, n = 7 control and n = 8
1166 Nlgn3$^{R451C/(y\ or\ R451C)}$ neurons). (J-K) Temporal patterns of spine shrinkage (n = 10
1167 control and n = 7 22q11.2$^{del/+}$ neurons, n = 5 control and n = 8 Setd1a$^{+/-}$ neurons, n = 8
1168 control and n = 8 Nlgn3$^{R451C/(y\ or\ R451C)}$ neurons). Statistical significance was determined
1169 using the Wilcoxon rank sum test for two independent samples (A-F) or two-way
1170 ANOVA for genotype and time (G-L).
1171

1172

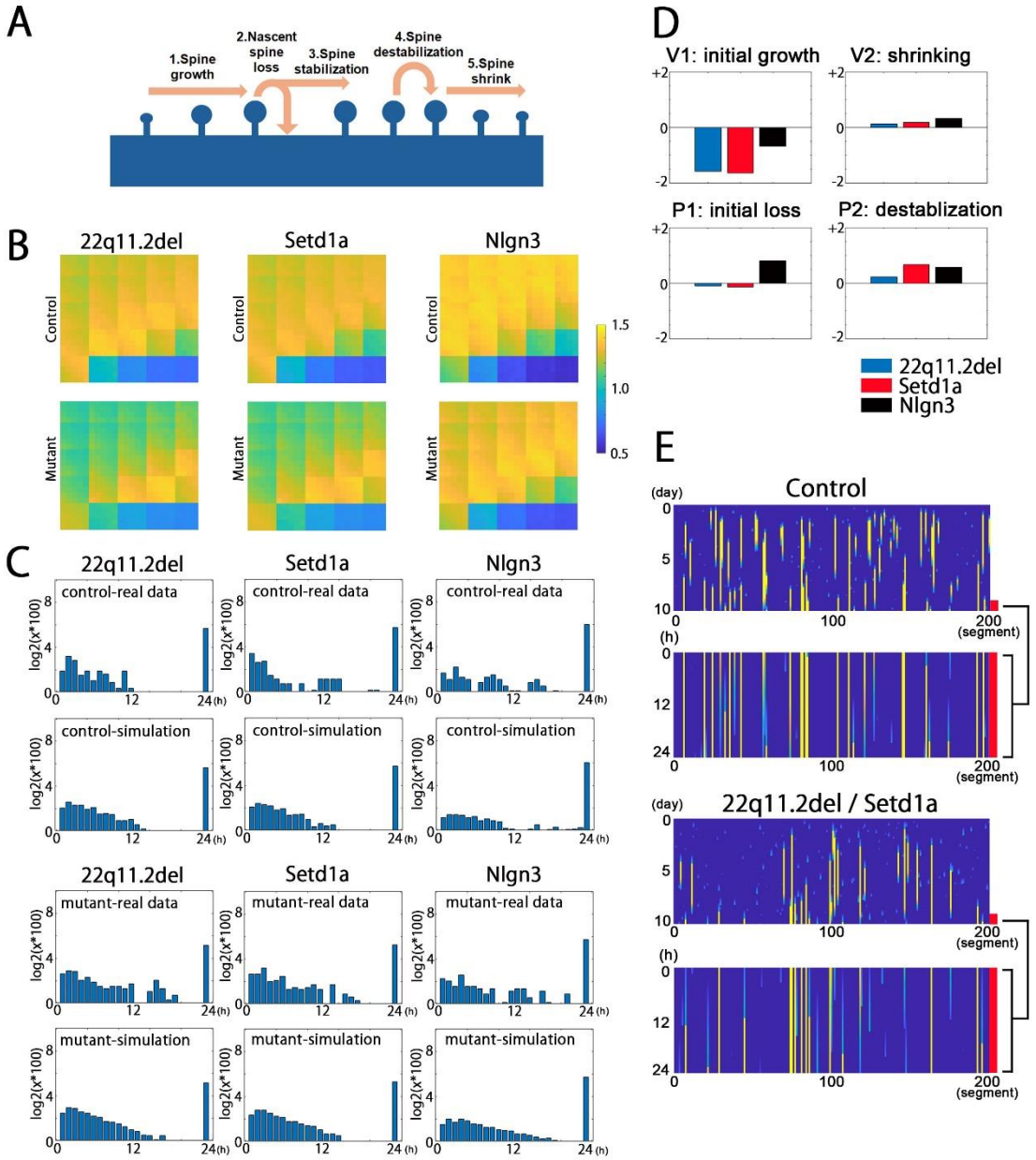

Figure 6

1173

1174

1175

1176

1177

1178 **Figure 6**

1179 Simulations of long-term spine turnover. (A) The model of spine dynamics. Five
1180 successive phases of spine state transitions were defined. Phase 1: newly formed
1181 spines grow at speed V1. Phase 2: nascent spines are eliminated with probability P1.
1182 Phase 3: nascent spines are stabilized when volume reaches an upper threshold.
1183 Phase 4: stable spines are destabilized with probability P2. Phase 5: spines shrinking
1184 at rate V2 are lost after reaching a lower threshold. (B) Pseudocolor maps of 625
1185 different combinations of these parameters to identify those best fitting the
1186 experimental data. (C) Frequency histograms of spine lifetimes for the three mouse
1187 models and controls (experimental data), and the results of simulations. The bin with a
1188 lifetime of 24 h corresponds to the spines that persisted throughout the imaging period.
1189 (D) Differences in V1, V2, P1, and P2 between mutant mice and controls. (E) Plots of
1190 individual spine turnover simulated using parameters that best fit the experimental data
1191 from control and schizophrenia mouse models. The upper plots show the progression
1192 of spine formation along 200 dendritic segments (50 μm) over 10 days. The lower plots
1193 show the enlargement of the last 24 h of spine turnover.
1194

1195

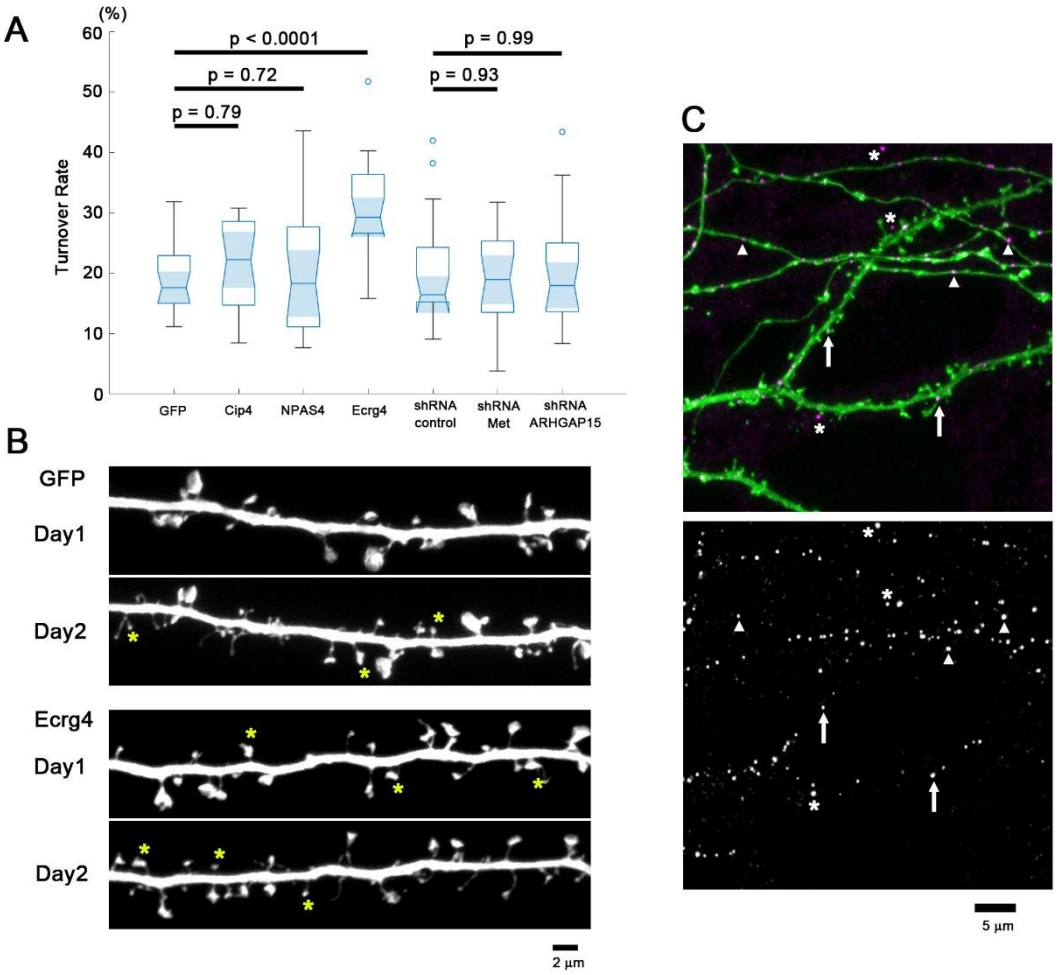

Figure 7

1196

1197

1198

1199

1200

1201

1202

1203

1204

1205 **Figure 7**

1206 Manipulation of candidate gene expression in wild-type hippocampal neurons and its
1207 effects on spine turnover. (A) Turnover rates of dendritic spines in neurons transfected
1208 with an overexpression plasmid encoding Cip4, Npas4, or Ecrg4, or a plasmid
1209 encoding an shRNA targeting Met or Arhgap15, together with a GFP expression
1210 plasmid. Spine turnover rates were calculated from the images of GFP-expressing
1211 dendrites taken at an interval of 24 h. Among the five DEGs, only the upregulation of
1212 Ecrg4 selectively increased the spine turnover rate. Statistical significance was
1213 determined by one-way ANOVA with post hoc Dunnett's tests between groups (results
1214 from n = 22 dendrites from 11 neurons for all conditions except the Met siRNA groups
1215 where n = 21 dendrites from 11 neurons were included in the analysis). (B)
1216 Fluorescence images of dendritic segments expressing GFP or GFP plus Ecrg4 on
1217 days 1 and 2. Newly formed spines are marked by asterisks. Bar, 2 μm. (C) Images of
1218 dendrites and axons expressing HA-tagged Ecrg4 together with GFP. Anti-HA
1219 immunocytochemistry revealed the presence of immunopositive puncta both in the
1220 dendrites (arrows) and axons (arrowheads). Some clusters could be detected in the
1221 extracellular space (asterisks). The upper image is the overlay of the anti-HA signal
1222 (magenta) and GFP (green). The lower image shows the distribution of the anti-HA
1223 signals. Bar, 5 μm.
1224

1225

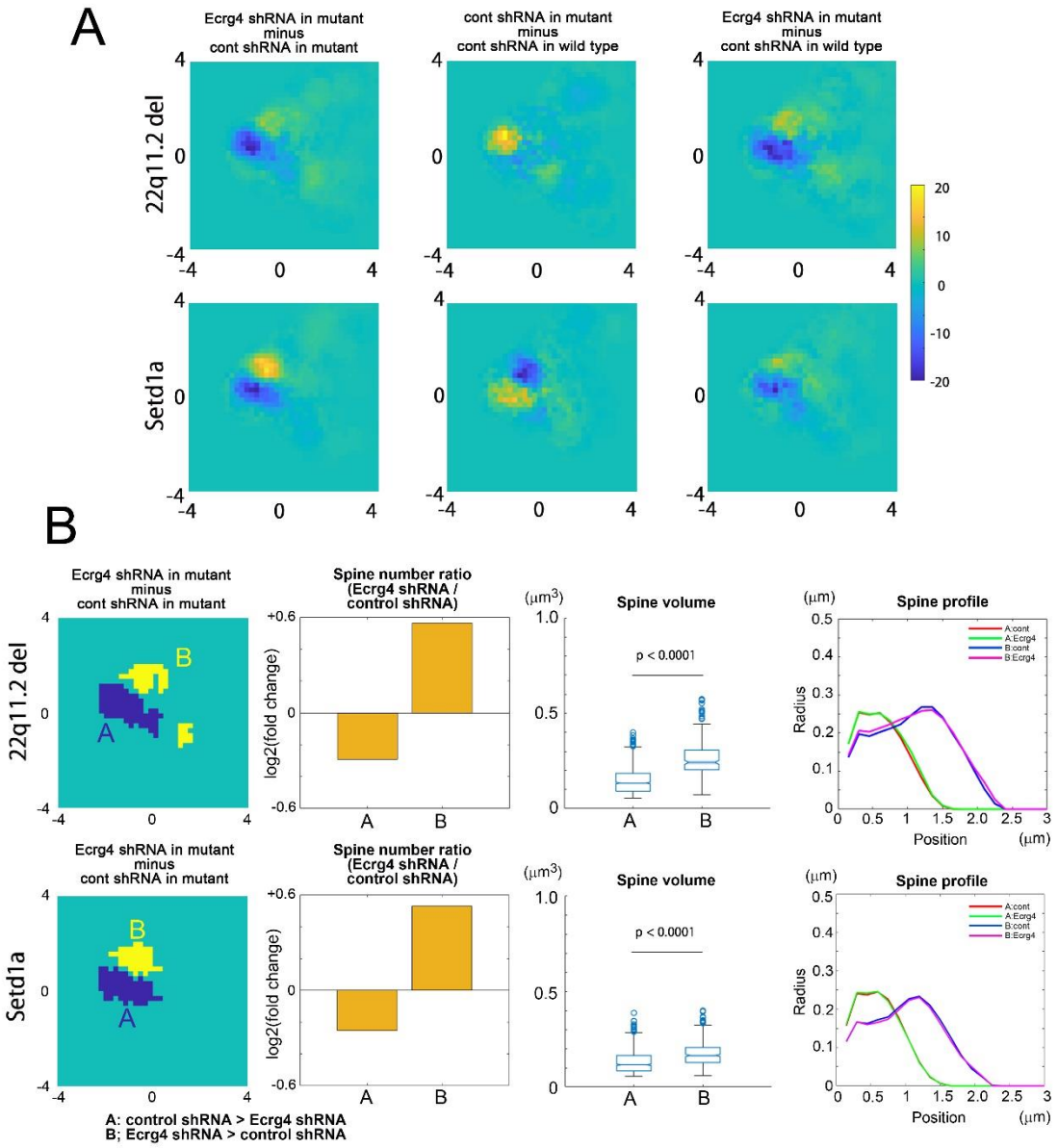

Figure 8

1226

1227

1228

1229

1230

1231 **Figure 8**

1232 Altered spine population profiles after suppression of Ecrg4 expression in neurons
1233 derived from schizophrenia mouse models. (A) Transfection of the Ecrg4-shRNA
1234 plasmid or control shRNA plasmid into neurons derived from 22q11.2$^{del/+}$ and Setd1a$^{+/-}$
1235 mice altered the subtracted density plots of spine populations. The left plots show the
1236 effect of Ecrg4 shRNA on the mutant background. The middle plots show the
1237 differences between mutant and wild-type neurons both expressing control shRNA. The
1238 right plots show the difference between mutant neurons expressing Ecrg4 shRNA and
1239 wild-type neurons expressing control shRNA. (B) Morphological properties of spines
1240 enriched in neurons derived from 22q11.2$^{del/+}$ and Setd1a$^{+/-}$ mice after transfection with
1241 the Ecrg4 shRNA plasmid or the control shRNA plasmid. The areas with more spines
1242 following Ecrg4 silencing are marked as B, while the areas with fewer spines are
1243 marked as A. The spine volume was larger in area B for neurons derived from both
1244 22q11.2$^{del/+}$ and Setd1a$^{+/-}$ mice. Statistical significance was determined using the
1245 Wilcoxon rank sum test (22q11.2$^{del/+}$, n = 1076 in area A and n = 230 in area B;
1246 Setd1a$^{+/-}$, n = 1142 in area A and n = 389 in area B). The profiles of spine radius along
1247 the long axis also confirmed the larger sizes of spines when Ecrg4 expression was
1248 downregulated by shRNA transfection. The numbers of spines and dendritic segments
1249 analyzed (in brackets) for the three conditions (mutant neurons expressing Ecrg4
1250 shRNA, mutant neurons expressing control shRNA, wild-type neurons expressing
1251 control shRNA) are as follows: 22q11.2$^{del/+}$; n = 968 (65), 954 (66), and 965 (66);
1252 Setd1a$^{+/-}$: n = 1,015 (66), 1,001 (66), and 1,168 (66).

1253

1254 **Supplementary Figures and Legends**

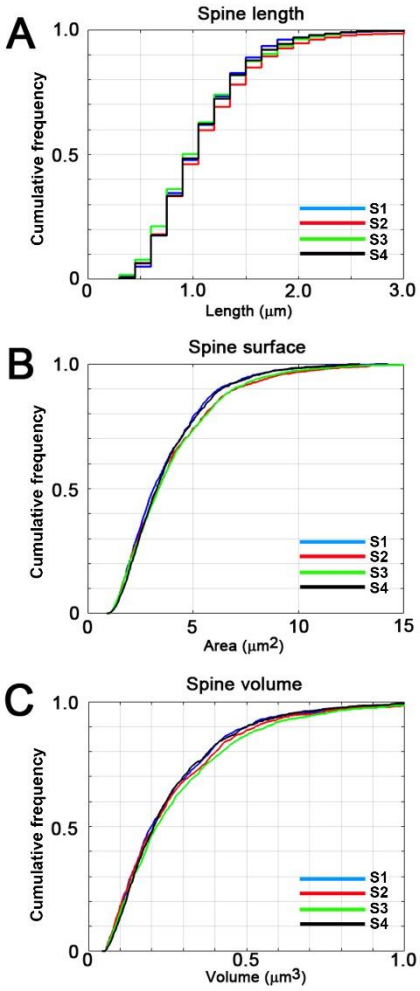

Supplementary Figure 1

1255

1256 **Supplementary Figure 1**

1257 Cumulative frequency plots of spine length, surface area, and volume measured in four

1258 independent experiments performed > 2 months apart. The cumulative frequency

1259 profiles shown as A to D were derived from mouse models Nlgn3$^{R451C/(y\ or\ R451C)}$ (S1),

1260 Syngap1$^{+/-}$ (S2), POGZ$^{Q1038R/+}$ (S3), and 15q11-13$^{dup/+}$ (S4). The Kolmogorov–Smirnov

1261 test detected significant differences in only three of 18 possible pairwise comparisons,

1262 surface area of (S1) vs. (S3) ($p = 0.017$), volume of (S1) vs. (S3) ($p = 0.032$), and

1263 volume of (S3) vs. (S4) ($p = 0.038$).

1264

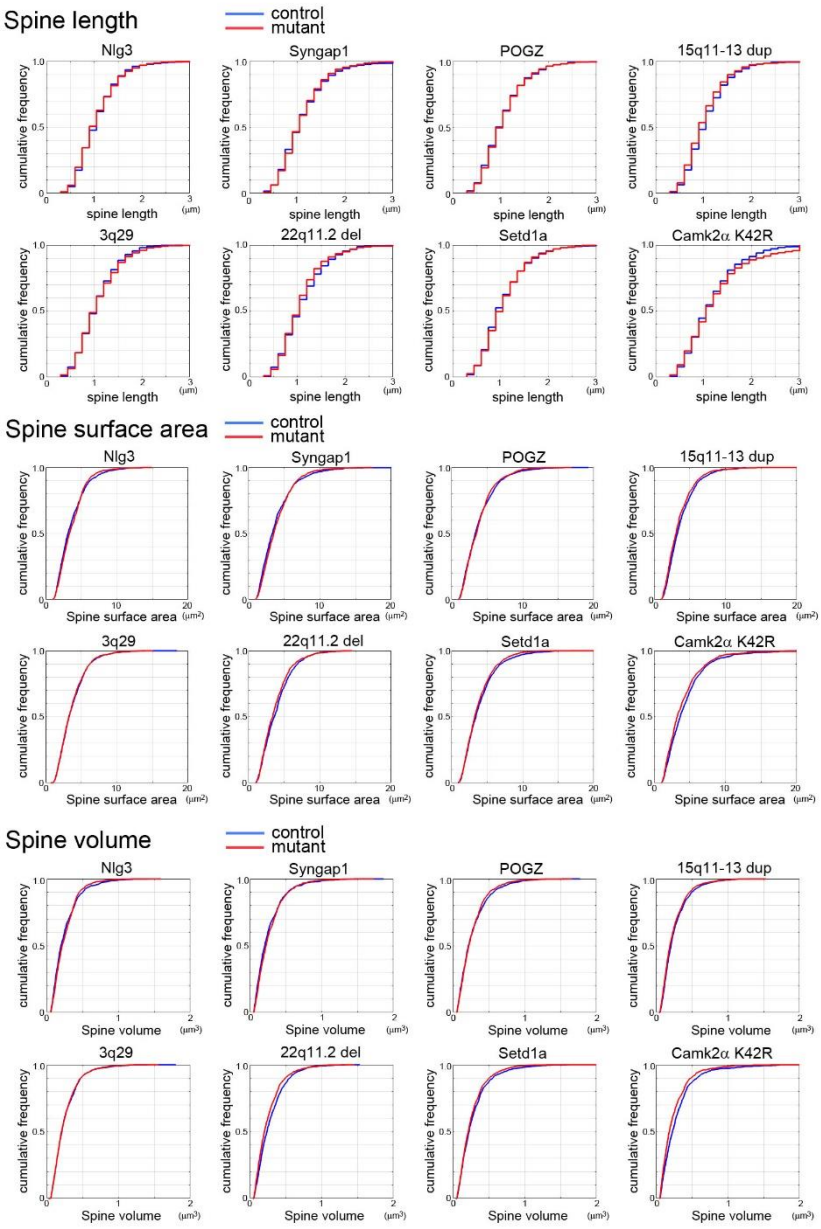

Supplementary Figure 2

1265

1266 **Supplementary Figure 2**

1267 Cumulative frequency plots of spine length, surface area, and volume for the eight

1268 mouse mutants; Nlgn3$^{R451C/(y\ or\ R451C)}$, Syngap1$^{+/-}$, POGZ$^{Q1038R/+}$, 15q11-13$^{dup/+}$, 3q29$^{del/+}$,

1269 22q11.2$^{del/+}$, Setd1a$^{+/-}$, and CaMKIIα$^{K42R/K42R}$.

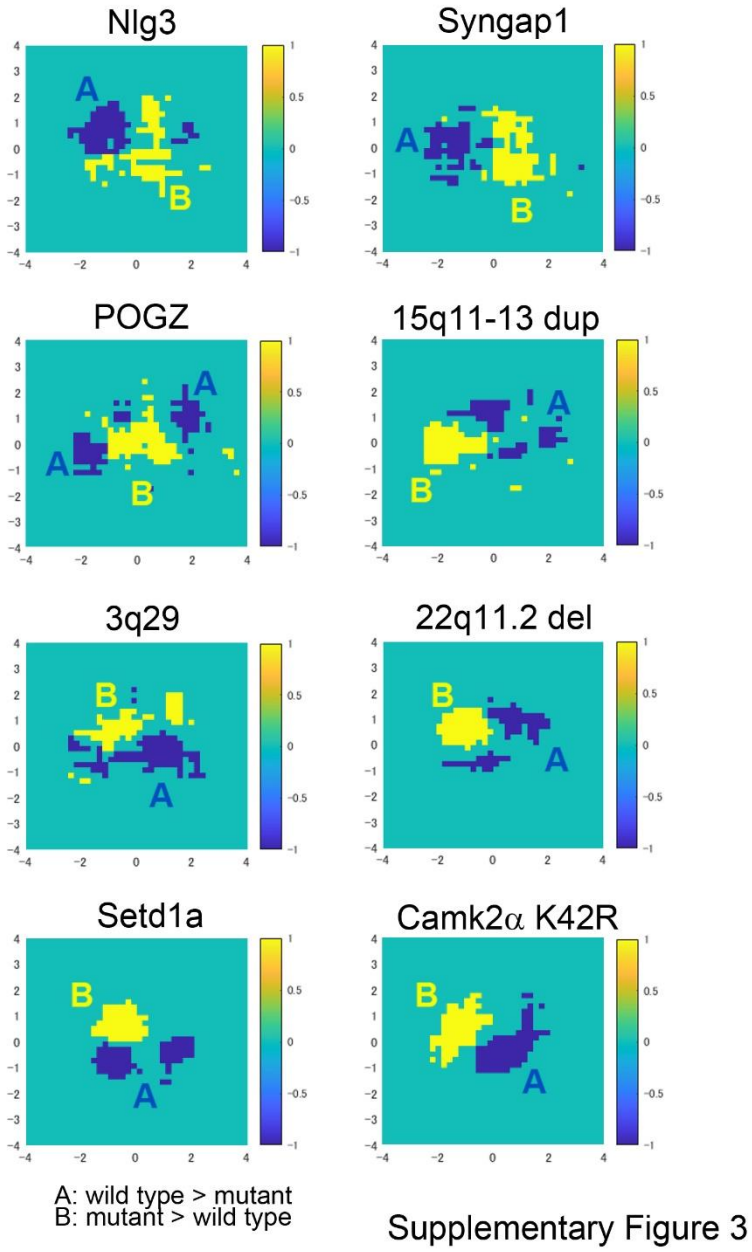

Supplementary Figure 3

Areas where control (A: blue) or mutant (B: yellow) spines show a higher density within the feature space of the PC1-PC2 plane. The plots for all 8 mouse models are presented.

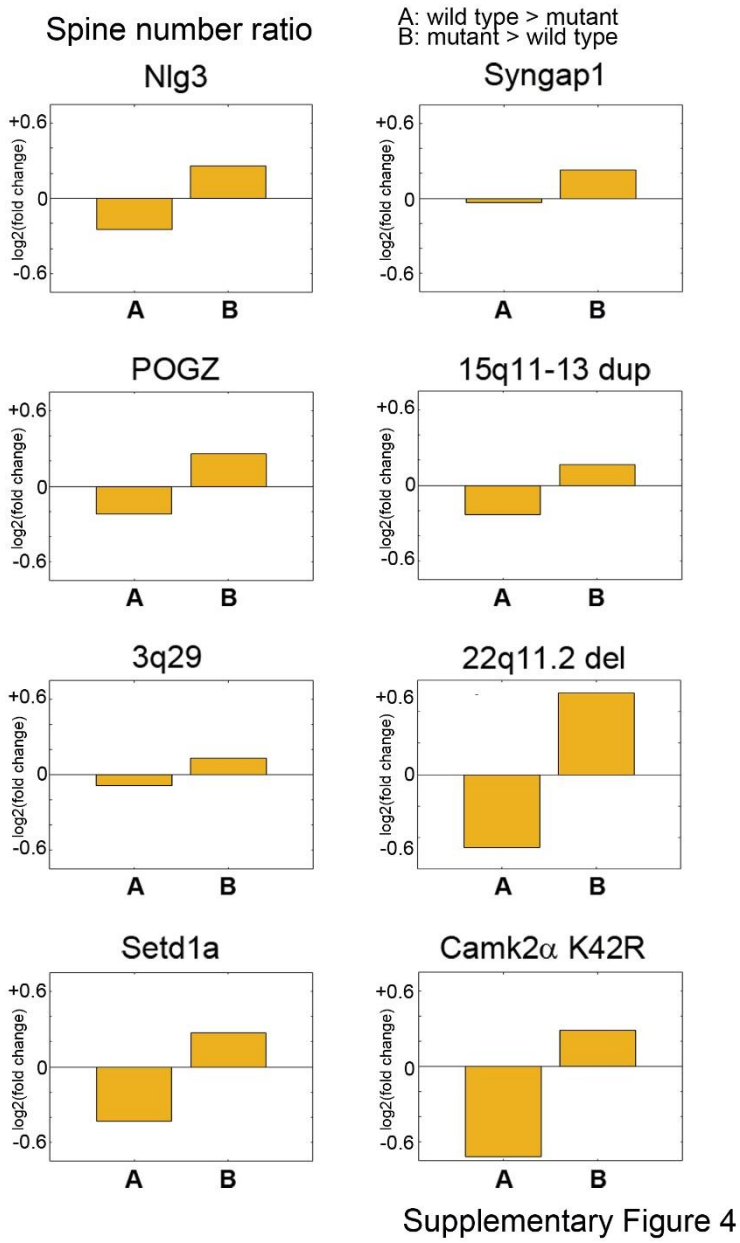

Supplementary Figure 4

The relative numbers of spines within areas A and B in the feature space from Supplementary Figure 3. The densities of mutant spines were higher in area B than in area A.

1283

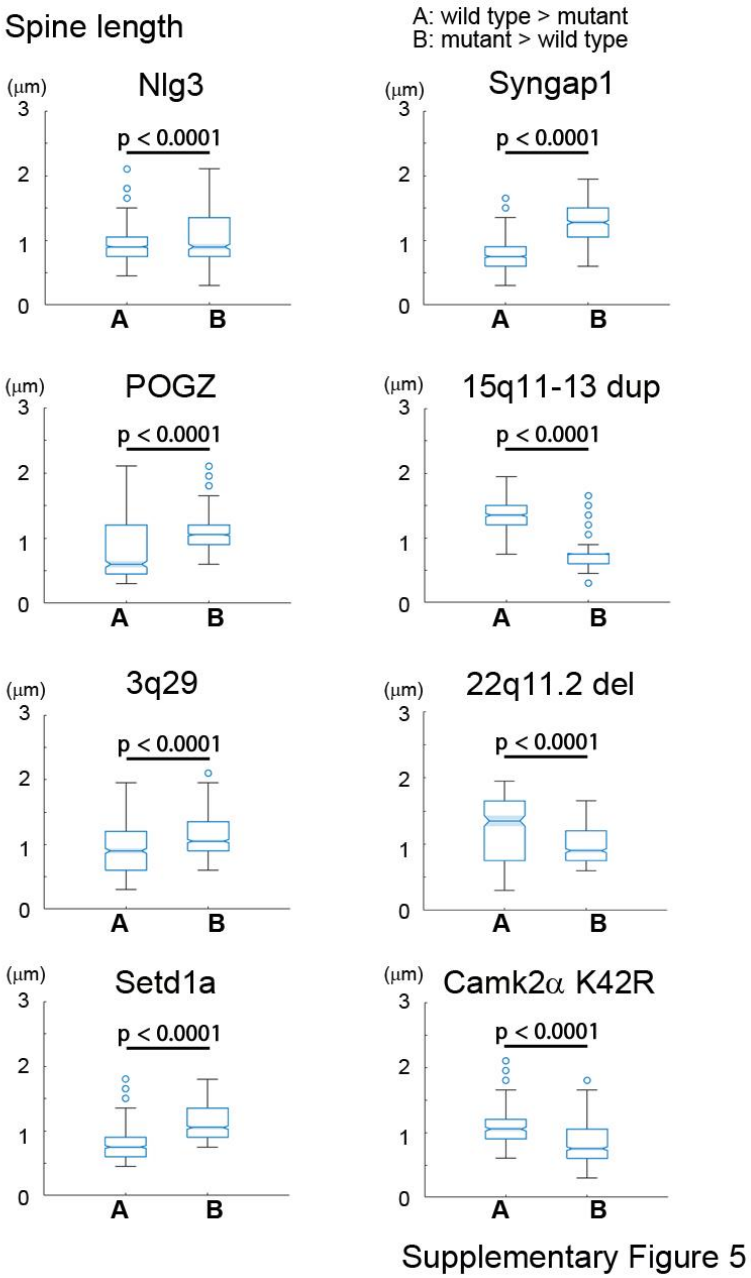

1284

1285

1286 **Supplementary Figure 5**

1287 Spine lengths within areas A and B from Supplementary Figure 3. For three ASD

1288 mouse models (Nlgn3$^{R451C/(y\ or\ R451C)}$, Syngap1$^{+/-}$, and POGZ$^{Q1038R/+}$) and two

1289 schizophrenia mouse models (3q29$^{del/+}$ and Setd1a$^{+/-}$), spines in mutant-dominant area
1290 B were longer than in area A. For one ASD mouse model (15q11-13$^{dup/+}$) and two
1291 schizophrenia mouse models (22q11.2$^{del/+}$ and CaMKIIα$^{K42R/K42R}$), spines in mutant-
1292 dominant area B were shorter than in area A. Statistical significance was determined
1293 by the Wilcoxon rank sum test. The numbers of control and mutant spines included in
1294 the analysis are as follows: Nlgn3$^{R451C/(y\ or\ R451C)}$, n = 775 in area A and n = 513 in area
1295 B; Syngap1$^{+/-}$, n = 668 in area A and n = 500 in area B; POGZ$^{Q1038R/+}$, n = 580 in area
1296 A and n = 815 in area B; 15q11-13$^{dup/+}$, n = 378 in area A and n = 797 in area B;
1297 3q29$^{del/+}$, n = 627 in area A and n = 824 in area B; 22q11.2$^{del/+}$, n = 308 in area A and n
1298 = 575 in area B; Setd1a$^{+/-}$, n = 472 in area A and n = 808 in area B; CaMKIIα$^{K42R/K42R}$, n
1299 = 237 in area A and n = 634 in area B.
1300
1301

1302

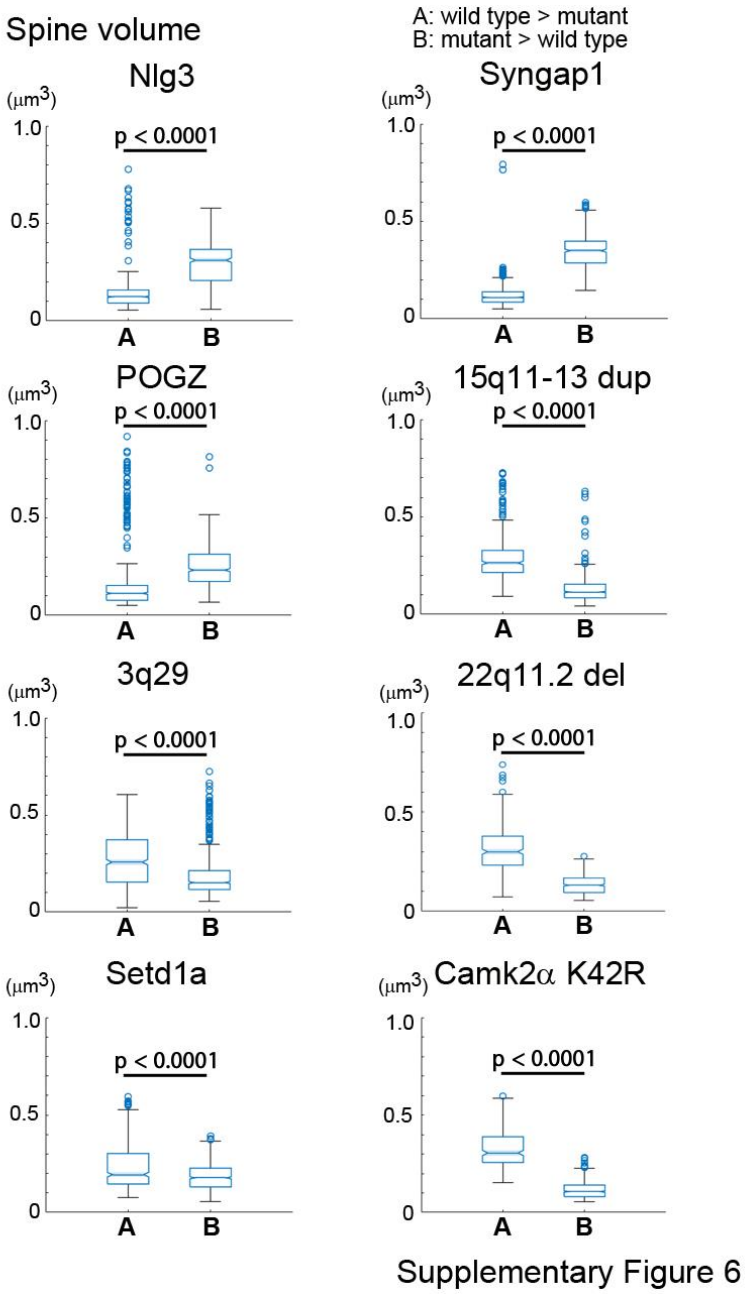

1303

1304 **Supplementary Figure 6**

1305 Spine volumes within areas A and B from Supplementary Figure 3. For three ASD

1306 mouse models (Nlgn3$^{R451C/(y\ or\ R451C)}$, Syngap1$^{+/-}$, and POGZ$^{Q1038R/+}$), spines in mutant-

1307 dominant area B were larger than in area A. For one ASD mouse model (15q11-13$^{dup/+}$)

1308 and four schizophrenia mouse models (3q29$^{del/+}$, 22q11.2$^{del/+}$, Setd1a$^{+/-}$; and

1309 CaMKIIα$^{K42R/K42R}$), spines in mutant-dominant area B were smaller than in area A.

1310 Statistical significance was determined using the Wilcoxon rank sum test. The numbers

1311 of spines included in the analysis are provided in the legend for Supplementary Figure

1312 5.

1313

1314

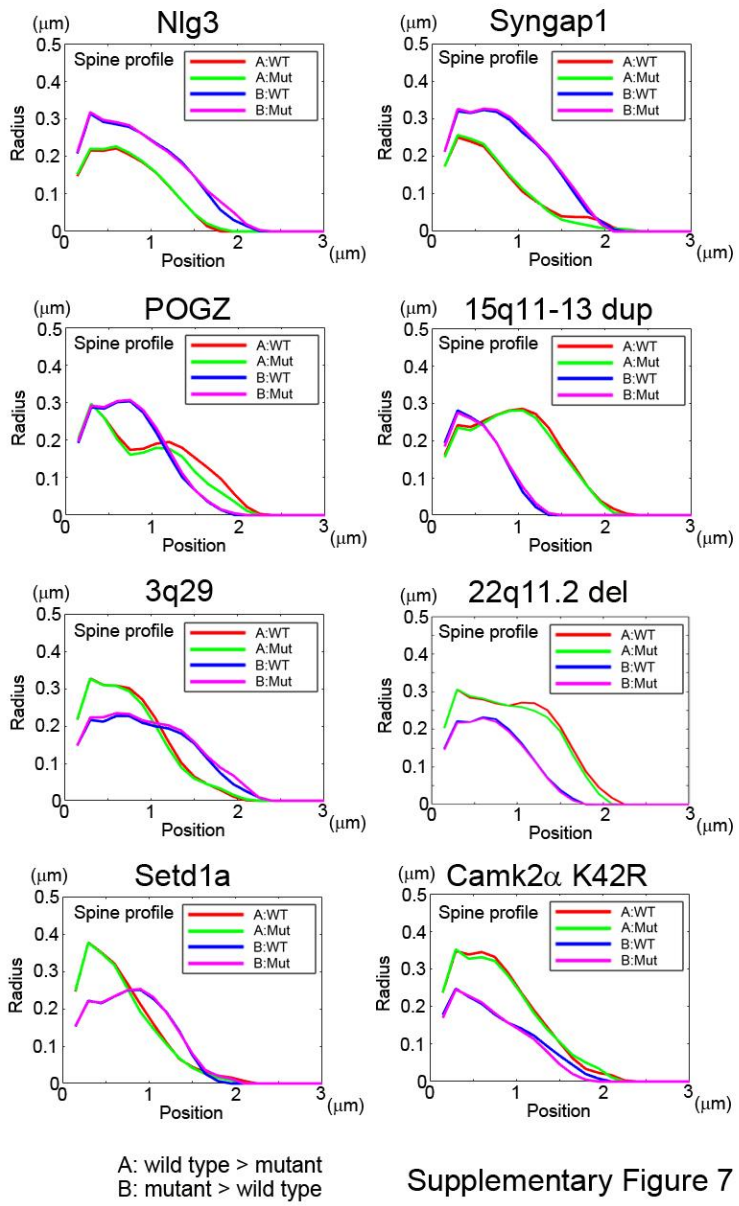

1315

1316

1317 **Supplementary Figure 7**

1318 Profiles of different spine populations (spines in the control-dominant area A and the

1319 mutant-dominant area B for both wild-type and mutant neurons) were visualized by

1320 plotting the radius along the long axis. Spine numbers included in the analysis are the

1321 same as in Supplementary Figure 5.

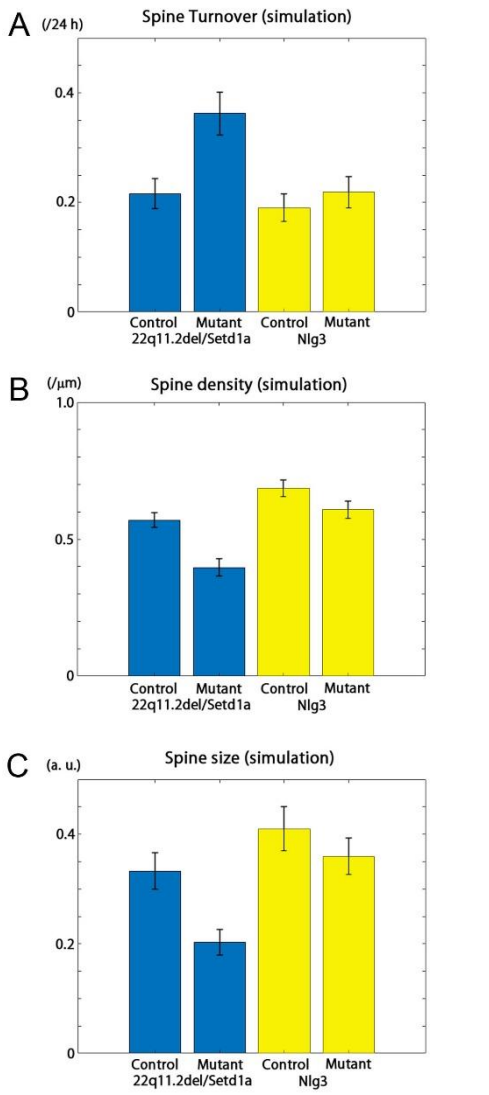

Supplementary Figure 8

Supplementary Figure 8

Spine turnover (A), density (B), and size (C) from simulation data. Simulation parameters were tuned to fit experimental results from control and mutant models. Means and standard deviations are shown.

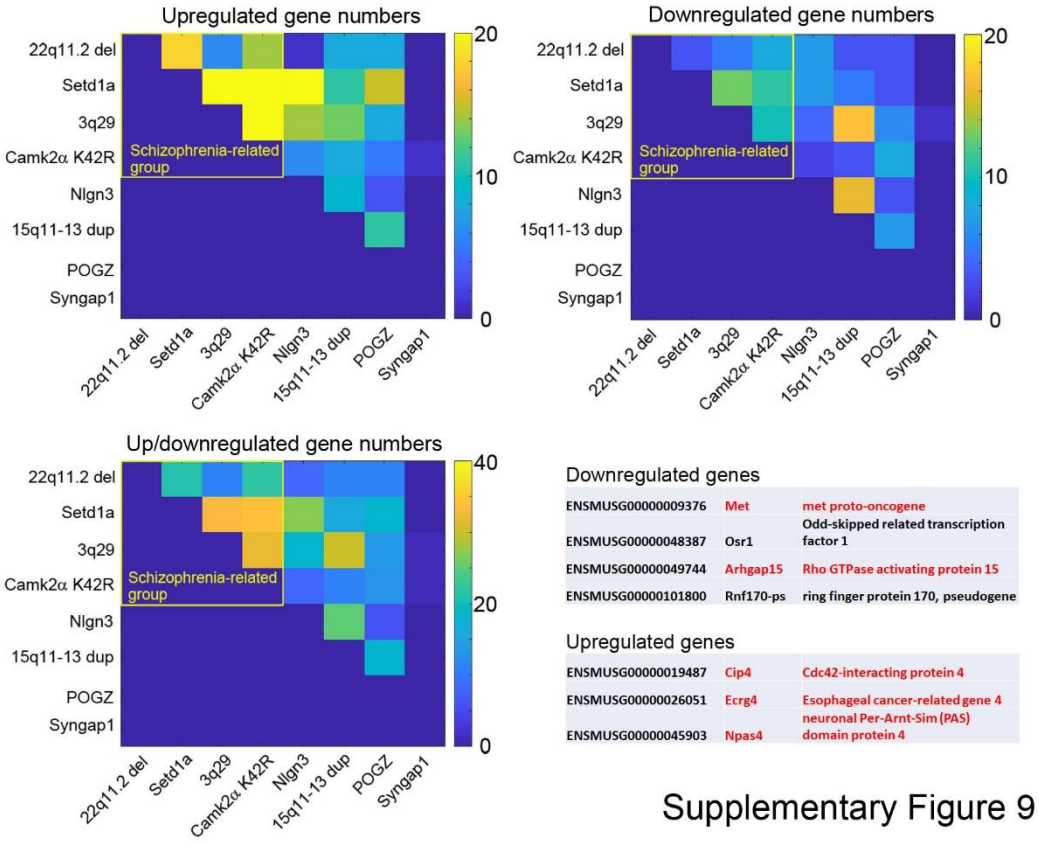

Supplementary Figure 9

Supplementary Figure 9

Pseudocolor presentation of differentially expressed genes (DEGs) between mutant and corresponding control mice. The number of shared DEGs was higher in the schizophrenia-related mouse models than in the ASD-related mouse models. Mouse gene identifiers (ENSMUSG) and gene names for DEGs shared by more than two schizophrenia mouse models and not differentially expressed in ASD mouse models are presented. DEGs analyzed for their effects on spines are in red characters.

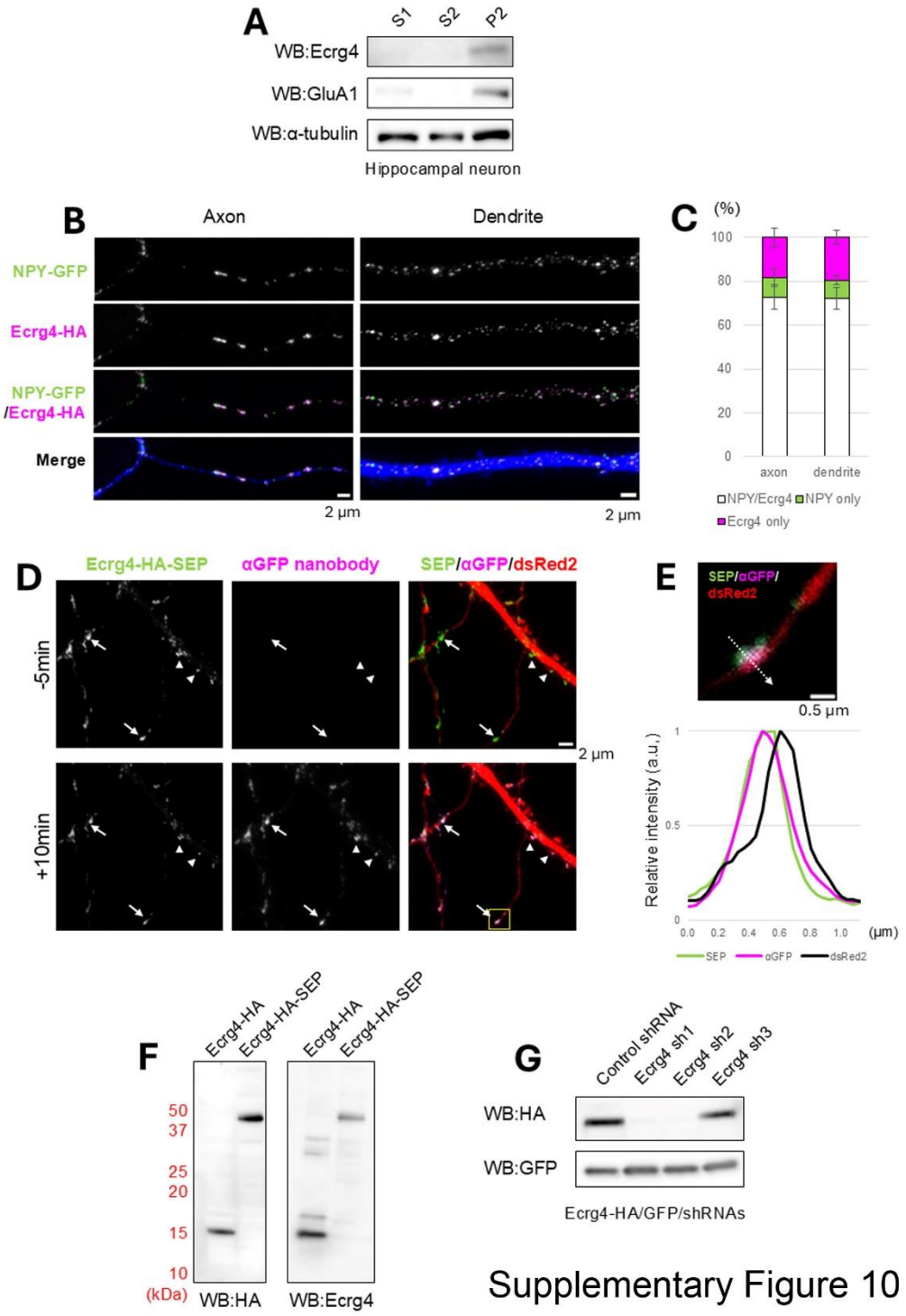

Supplementary Figure 10

1346 **Supplementary Figure 10**

1347 Expression and distribution of Ecrg4 in cultured hippocampal neurons. (A) Preferential
1348 localization of Ecrg4 protein in the membrane fraction. Immunoblotting of Ecrg4,
1349 GluA1AMPA-type glutamate receptor, and α-tubulin in the remaining fraction after
1350 removal of nuclei (S1), supernatant after centrifugation (S2), and resulting pellet (P2).
1351 (B) Images of an immunostained hippocampal neuron expressing HA-tagged Ecrg4
1352 and NPY-GFP. The fluorescence signals were partially colocalized, suggesting Ecrg4
1353 protein accumulation in dense-core vesicles. Bar = 2 μm. (C) Quantification of the
1354 overlap between puncta immunopositive for HA-tagged Ecrg4 and NPY-GFP. N = 4
1355 cells from 1 dish. (D) Surface labeling with the anti-GFP nanobody revealing clusters of
1356 SEP-tagged Ecrg4 in dsRed2-positive axons (arrows) and dendrites (arrowheads). A
1357 nanobody was applied at time t = 0 min. Bar = 2 μm. (E) Enlarged image of a single
1358 Ecrg4 puncta in the axon, marked by a yellow square in (D), with the fluorescence
1359 intensity profile along the dashed arrow. Bar = 0.5 μm. (F) Immunoblotting of Ecrg4-HA
1360 or Ecrg4-HA-SEP in total cell lysates from COS-7 cells. The molecular weights of these
1361 exogenously expressed proteins detected using anti-HA and anti-Ecrg4 antibodies
1362 were consistent with those of Ecrg4-HA (18 kDa) and Ecrg4-HA-SEP (45 kDa). (G)
1363 Reduced Ecrg4-HA protein expression by transfection of Ecrg4 sh1 or sh2 in COS-7
1364 cells expressing Ecrg4-HA and GFP. Bars, 5 μm.

1365

1366

1367

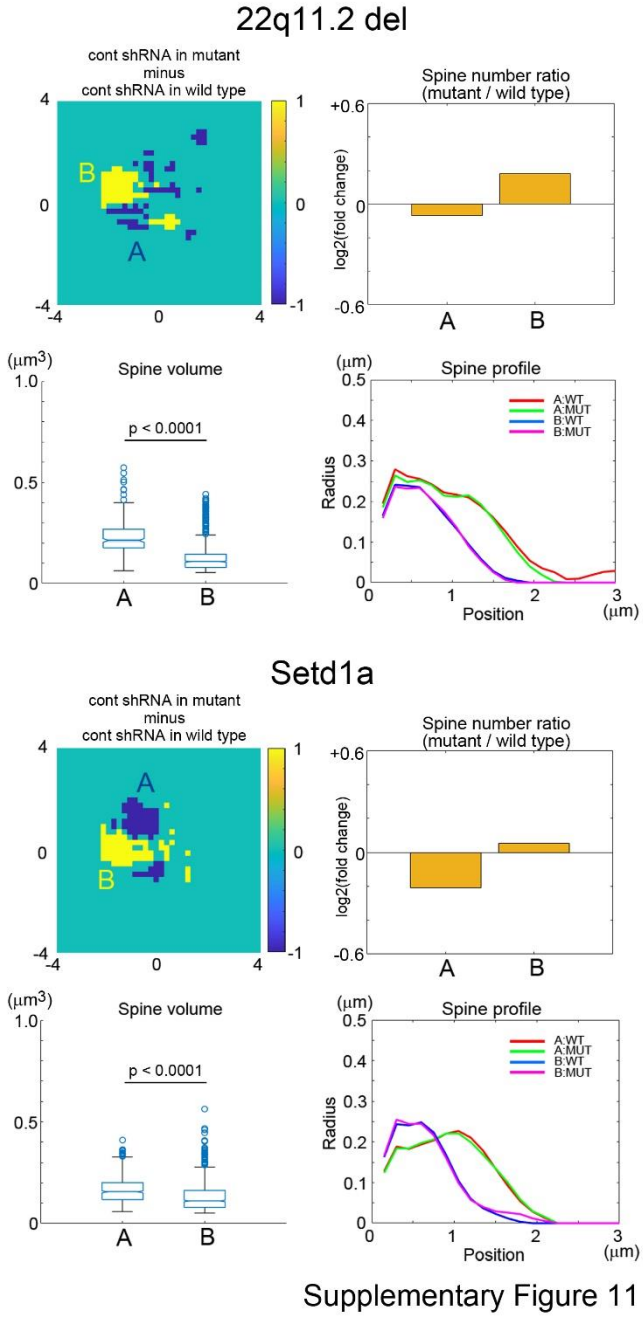

Supplementary Figure 11

1368

1369 **Supplementary Figure 11**

1370 Subtracted density plots between neurons from schizophrenia model mice (22q11.2$^{del/+}$

1371 and Setd1a$^{+/-}$) and neurons from wild-type mice both expressing control shRNA. A

1372 comparison of the spine populations within control-dominant area A and mutant-

1373 dominant area B revealed smaller spine volumes in area B. The spine profiles along

1374 the long axis revealed an elongated morphology in area A for both 22q11.2$^{del/+}$ and

1375 Setd1a$^{+/-}$ mutant mice. Statistical significance was determined using the Wilcoxon rank

1376 sum test (22q11.2$^{del/+}$, n = 237 in area A and n = 789 in area B; Setd1a$^{+/-}$, n = 630 in

1377 area A and n = 937 in area B).

1378

1379